Journal of Hydrology: Regional Studies 54 (2024) 101856

Contents lists available at ScienceDirect

Journal of Hydrology: Regional Studies

journal homepage: www.elsevier.com/locate/ejrh

Component separation and origin estimation of mining-influenced water based on fluoride ions and water isotopes in underground legacy mine, Central Japan

Shinji Matsumoto [a,*], Taiki Katayama [a], Tetsuo Yasutaka [a], Shingo Tomiyama [b], Saburou Yamagata [c]

[a] Geological Survey of Japan, National Institute of Advanced Industrial Science and Technology (AIST), Central 7, 1-1-1 Higashi, Tsukuba, Ibaraki 305-8567, Japan
[b] Faculty of Engineering, Hokkaido University, Kita 13 Nishi 8, Sapporo 060-8628, Japan
[c] Mitsubishi Materials Corporation, 3-2-3, Marunouchi, Chiyoda-ku, Tokyo 100-8117, Japan

ARTICLE INFO

Keywords:
Mining-influenced water
Surface water
Groundwater
underground mine
fluoride ions
water isotopes

ABSTRACT

Study region: A legacy underground tungsten mine in a mountainous area, central Japan.
Study focus: We analyzed mining-influenced water (MIW) from mine voids and surface water from rivers to determine the dissolved ion concentrations and water isotopes ($\delta^{18}O$ and $\delta^{2}H$). The results were interpreted using principal components and cluster analyses, as well as Eh-pH (Pourbaix) diagram. By integrating the obtained analytical results with mine-related data, we conducted component separation of MIW and estimation of their origins.
New hydrological insights for the region: The MIW and part of surface water were characterized by the SO_4^{2-} and F^- generated via the dissolution of sulfide minerals and fluorite (CaF_2) from the ore deposit. MIW components were successfully separated using these indicators and water isotopes. The results of component separation indicated that the MIW consisted of two components, namely infiltrating water that rapidly passes through upper mine voids to reach the mine void at ground level, and groundwater that undergoes some degree of residence time before flowing into the ground level void from shaft I.

1. Introduction

Mine drainage can damage the surrounding environment if inadvertently released directly into the environment (Nordstrom et al., 2015; Younger, 2001; Blowes et al., 2003). Mining-influenced water (MIW) has conventionally been treated as wastewater for environmental preservation in over 80 legacy mines in Japan—approximately half of which are closed mines without liable parties (Iwasaki et al., 2021; Koide et al., 2012). As more than 80 % of Japan's terrain is mountainous, most closed or abandoned mines (legacy mines) were established through underground mining in mountainous regions (Hamabe and Yano, 1976; Nishimoto et al., 2021).

Abbreviations: [1] d-excess, deuterium excess; DO, dissolved oxygen; EC, electrical conductivity; $E_{S.H.E.}$, standard hydrogen electrode; GWB, Geochemist's Workbench; MIW, mining-influenced water; ORP, oxidation-reduction potential; PCA, principal component analysis; SI, saturation index; TDS, total dissolved solids; VSMOW, Vienna Standard Mean Ocean Water.

* Corresponding author.
E-mail address: shin.matsumoto@aist.go.jp (S. Matsumoto).

https://doi.org/10.1016/j.ejrh.2024.101856
Received 13 March 2024; Received in revised form 27 May 2024; Accepted 1 June 2024
Available online 17 June 2024

Considering the pivotal function of upstream water resources in mountainous areas as vital recharge sources for downstream water systems, the MIW discharges from legacy mines into upper stream pose a significant threat to downstream water resources (Peachey, 2004; Sracek et al., 2012; Yoon et al., 2015). Therefore, the implementation of effective management and treatment strategies for MIW is essential for watershed-based management of water resource (Hardy, and Koontz, 2008; Northey et al., 2019).

Hydrological data can be used to determine efficient measures for treatment or source control, or both, for MIW (Nishimoto et al., 2021; Skousen et al., 2017; Taylor et al., 2005; Trumm, 2010; Valkanas and Trun, 2018). Despite the abundance of hydrological data during mine development, mining activities can alter the hydrological systems (El Fahem et al., 2021; Newman et al., 2017; Wang et al., 2021). Consequently, a hydrological reassessment is required to elucidate the complex dynamics of newly formed groundwater flow systems and the altered water quality after mining activities. Hydrological data regarding the sources of MIW and the pathways of inflow water into mine voids concern both the volume of mine effluent and fluctuations in water quality and are essential for conducting appropriate MIW treatment.

In this study, we segregated the components of MIW within the mine voids of legacy mines located in central Japan, based on water quality, isotopic data, and accumulated mine data on wastewater volume and mine tunnel distribution. Specifically, we investigated the infiltration of surface water into the underground mine voids and groundwater inflows, as well as the MIW pathways to assess the sources of MIW and track mine water inflows. Research on the geological features and quality of MIW had been conducted at this mine until the mine closure in the late 1900s (Ikeda et al., 1983; Seki, 1989; Ogasawara et al., 1993). Wastewater treatment commenced after the closure, although this treatment process continues. However, investigations into the origins of MIW within the mine voids after several decades of the mine closure have not been conducted. The findings of this study contribute to the accumulation of data regarding the types and pathways of inflow water within the geological context and mine voids distribution of this mine. Such data are necessary to discuss fluctuations in water quality and quantity of MIW during distinctive meteorological conditions, such as heavy rainfall or typhoons. Furthermore, geological features and distributions of mine voids vary across mines worldwide, hence the characteristics of MIW differ. In this context, this study provides novel insights into the relationship between variations in such environmental backgrounds and MIW characteristics.

2. Study area

The selected study area is a mountainous region and a legacy underground mine located in central Japan (Fig. 1a). The sampling points for surface water were denoted as W1–W29 (Figs. 1b and 1c). The mine site is located approximately 7 km from the primary river, which runs through points W27–W29. Historically, this mine was primarily developed for tungsten extraction through underground mining until the late 1900s (Ogasawara et al., 1993). MIW contains fluoride ions (F^-), attributed to the presence of fluorite (CaF_2) within the ore deposit, and has been continuously generated and treated to mitigate its environmental impact since the mine closure (Ikeda et al., 1983).

A detailed depiction of the mine site illustrates underground mine voids that are color-coded based on their depth levels and superimposed on the elevation map (Fig. 1d and Fig. 2). Sampling points for MIW within the mine voids were labeled as M1–M9. Blue

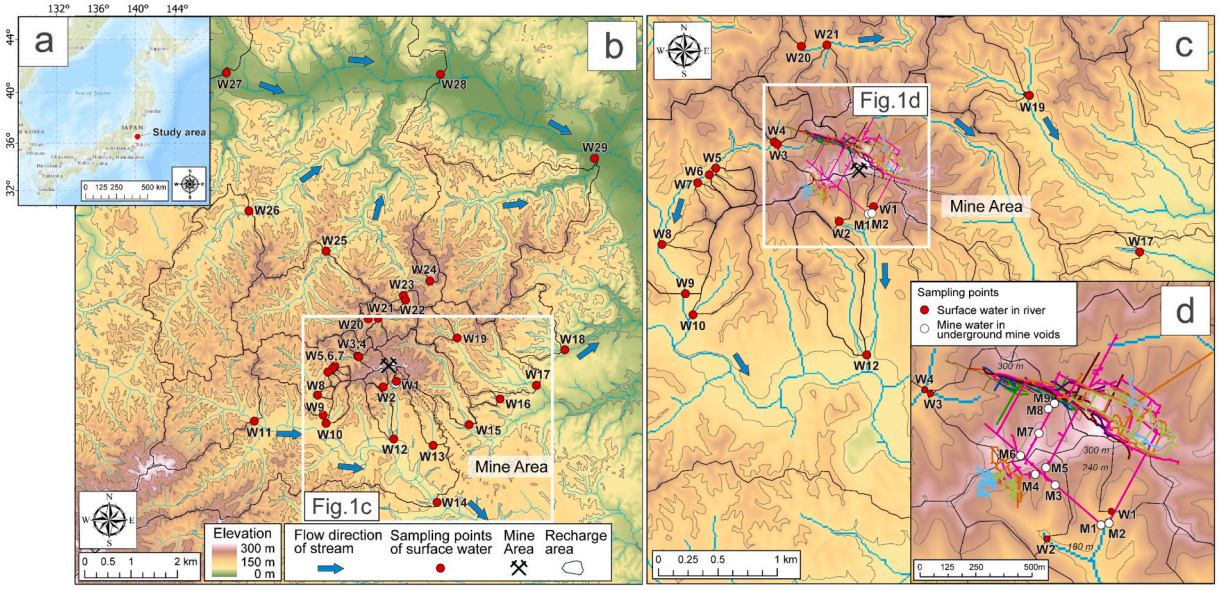

Fig. 1. (a–c) Topographical map of the study area with sampling points for surface waters (W1–W29) and MIW (M1–M9) and (d) spatial distribution of mine voids. The underground mine voids are color-coded based on their depth and superimposed on the topographical map. The sampling points for surface water and MIW are shown in red and white circles, respectively. The flow directions of the river, stream, and MIW are illustrated with blue arrows. The recharge area for each sampling point was illustrated by black lines.

arrows indicate the direction of river flow. The highest elevation point of the mine site is 355 m, with the voids situated beneath the mountain. The spatial distribution of underground mine voids was described along with a cross-sectional view of the A–A′ line (Fig. 2). The horizontal voids were constructed based on the ground level at an elevation of 170 m above sea level. These include upper-level voids, denoted as U1–U3, extending up to 230 m, as well as lower-level voids, designated as L1–L7, descending to −30 m. The lower-level voids interconnect via shafts I and II, as indicated in the A–A′ cross-section. Inflowing water from shaft I (M8) into the mine voids was observed with the water table at the ground level void. MIW is discharged from the adits at M1 and M2, as a mixture of MIW from M3 to M9, via a drainage channel within the ground level voids, and directed to an adjacent treatment plant.

After treating MIW at the treatment plant, the treated MIW is discharged into the river and flows toward the W14 sampling point. Water quality of the treated water meets the Japanese effluent standards. Based on the monitoring data from 2019 to 2020, the average flow rate of the MIW mixture at M1 and M2 ranged from 0.7 to 0.8 m^3/min. The average annual precipitation and mean annual temperature were 1366 mm/year and 13 °C, respectively, for 10 years from 2012 to 2021 (Japan Meteorological Agency). These data

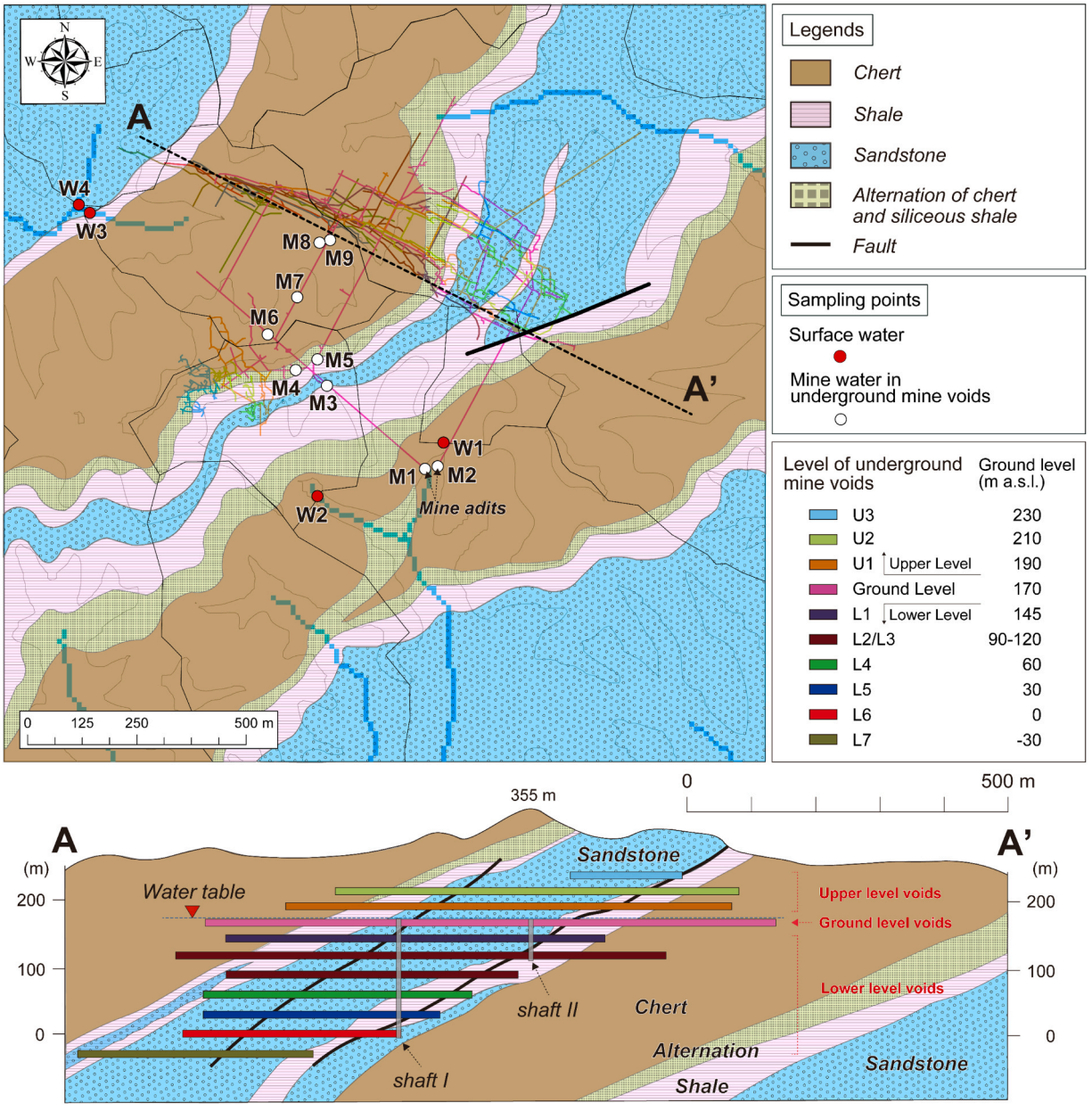

Fig. 2. Geological characteristics of the study area (figure adapted from Ikeda et al., 1983). The geological information is superimposed on the elevation map along with underground mine voids. The mine voids are classified into upper level (U1–U3) and lower level (L1–L7) based on ground level. The water table is located at ground level.

were recorded at point A, situated approximately 12 km north of the mine site, with an elevation of 95 m.

The geological composition of the study area comprises chert, shale, sandstone, and alternating layers of chert and silicious shale (Fig. 2) (Ikeda et al., 1983). Within this geological context, the ore deposits have a deep tungsten-copper-tin (W-Cu-Sn) vein formed within sandstone and shale layers, and sandwiched between two strata of chert. Predominant ore minerals within the deposit contain iron tungstate ($FeWO_4$), which coexists with chalcopyrite ($CuFeS_2$), pyrite (FeS_2), and other mineral species. Notably, the ore deposit contains fluorite, which characterizes the fluoride-rich MIW prevalent in this mine (Takase, 1958). Numerous large fractures, spanning several meters in width, have been identified inside the alternation of the sandstone and shale layers. These layers continue to the lower-level voids (L7). Additional minor faults are present within this underground mine, along with the fault lines shown in black (Fig. 2) (Ikeda et al., 1983).

The water table was situated within the ground level void, and the lower voids were filled with groundwater. The phenomenon where water bodies with different physical and chemical properties overlap in layers occurs even in flooded mines as stratification (Mugova and Wolkersdorfer, 2022; Nuttall and Younger, 2004). Stratification might have formed in the lower voids in this mine; however, investigations into this phenomenon are lacking. Moreover, remnants of collapsed scaffolding and heavy machinery from past mining activities exist within shaft I, which is accessible in this mine, making water sampling from this shaft challenging from a safety perspective.

3. Materials and methods

3.1. Water sampling

Surface water samples were collected at sites W1–W29 along the river and streams surrounding the mine area (Fig. 1b) in February and November of 2020, and August and October of 2021. Due to restricted access to origination points of spring and groundwater, as well as upstream river sections, surface water was collected from accessible upstream locations around the mine. Water samples were collected using 100 mL polypropylene bottles (Sanplatec Co., LTD, Osaka, Japan) and filtered through a 0.45 μm polyethersulfone filter at the site for laboratory analysis. The water samples were sealed, refrigerated at 4°C, and transported to the laboratory for further analysis. Additionally, the pH, oxidation-reduction potential (ORP), and temperature of water were measured using a pH meter (model 72–21JAA) (Yokogawa Electric Co. Ltd., Japan) equipped with a pH electrode (model pH72SN–21–AA) (Yokogawa Electric Co. Ltd., Japan) and an ORP electrode (model OR72SN–41–AA) (Yokogawa Electric Co. Ltd., Japan). Electrical conductivity (EC) was measured using a conductivity meter (model SC72) (Yokogawa Electric Co., Ltd.). The measured ORP value (E) was converted to the standard hydrogen electrode ($E_{S.H.E.}$) using the Nernst equation, which was provided by the operating manual of the portable meter (model pH72–21JAA), manufactured by Yokogawa Electric Co. Ltd., Japan. The calculated results were denoted as Eh.

MIW samples were collected at sites M1–M9 within the horizontal voids in July 2019, November 2020, and October 2021 (Figs. 1d and 2). Specifically, mine drainage samples were obtained from adits M1 and M2, while seepage water was gathered from the ceiling at site M3. MIW samples were obtained from drainage channels at sites M4–M7 and M9. Inflowing water into the ground level mine voids was sampled from shaft I at site M8. Given that shaft I accesses the lower levels of the voids (L1–L6), the dissolved oxygen (DO) concentration of the M8 sample was below 0.05 mg/L, as determined using a DO meter (model OM–71) (Horiba Co. Ltd., Japan) equipped with Clark–type sensor (model 9551–20D) (Horiba Co. Ltd., Japan). Moreover, pH, temperature, and EC were measured using the same equipment employed during surface water sampling. Each type of MIW sample was collected in 100 mL polypropylene bottles (Sanplatec Co., LTD, Osaka, Japan) and filtered through a 0.45 μm polyethersulfone filter at the site in preparation for laboratory analysis.

3.2. Geochemical and isotopic analysis

Several studies have been conducted to elucidate the origin of MIW, its flow paths, and the potential environmental impacts based on the geochemical or isotopic signatures, or both, of surface and groundwater around mines (Douglas et al., 2000; Doveri et al., 2021; Qin et al., 2021; Wang et al., 2021; Zheng et al., 2019). Thus, we utilized both geochemical and isotopic approach for investigating surface water and MIW in this study. The collected water samples were subjected to ion chromatography (Dionex ICS-6000; Thermo Scientific, USA) to quantify the concentration of dissolved ions (F^-, Na^+, K^+, Ca^{2+}, Mg^{2+}, Cl^-, SO_4^{2-}, and NO_3^-), with an analytical error of ±5 %. Additionally, the Fe concentration was determined using inductively coupled plasma mass spectrometry (ICP-MS, NexION 300, PerkinElmer, USA) after adding 1 % HNO_3 by weight. The detection limit was 0.0001 μg/L, which is described in the manual.

The alkalinity was measured via titration with 0.02 N H_2SO_4, and the results were converted to the HCO_3^- concentration with an analytical error of ±10 %.

The Durov diagram is a graphical representation used to visualize water quality based on major anions and cations in addition to pH and total dissolved solids (TDS) (Ben Brahim et al., 2013; Durov, 1948). The analytical results were plotted on a Durov diagram along with pH and TDS to classify the water quality characteristics. TDS parameters were obtained via calculation using the Geochemist's Workbench (GWB 12) (Aqueous Solutions LLC) (Bethke et al., 2022). Furthermore, the GWB was utilized to conduct hydrogeochemical modeling for surface water and MIW in the study area, which calculated the mineral saturation index (SI) and constructed the Pourbaix diagram (Pourbaix, 1966).

The stable isotope ratio of oxygen and hydrogen ($\delta^{18}O$ and $\delta^{2}H$) was analyzed using wavelength-scanned cavity ring-down spectroscopy equipped with a liquid water isotope analyzer (L2120-i, Picarro Inc., Sunnyvale, CA, USA). The isotope ratios were expressed as thousand fractions of Vienna Standard Mean Ocean Water (VSMOW). The analytical errors were ±0.10 ‰ for $\delta^{18}O$ and

±1.0 ‰ for δ^2H. The deuterium excess (d-excess) was computed using the formula "d-excess = $\delta^2H - 8 \times \delta^{18}O$" based on the obtained results (Dansgaard, 1964)

3.3. Calculation of recharge area and elevation

The recharge area of each sampling point was determined by analyzing the topographic gradient using ArcGIS Pro 2.9 (ESRI, USA) as depicted by the black lines (Fig. 1b, c, d and Fig. 2). The mean elevation within the upstream catchment area was determined as the calculated recharge elevation of the sampling points. Subsequently, the relationship between the calculated recharge elevation and water isotopes was examined to explore altitude effects (Clark and Fritz,1997; Kong and Pang, 2016).

To estimate recharge elevations through the altitude effect utilizing water isotopes, it is preferable to utilize springs and/or groundwater sources with a certain residence time, ensuring the homogenization of evaporation effects and variations in isotope values across rainfall events (Doveri et al., 2021; Huang et al., 2020). However, constraints in the study area, such as inaccessible spring sites or limited groundwater sampling locations, may preclude the availability of such data. In contrast, surface water, being accessible and readily collectible, presents a viable alternative. While the utilization of surface water isotopes has been applied to estimate recharge elevations (Levy et al., 2020; McGill et al., 2020; Nishimoto et al., 2021), the elevation vs. isotope relationship may not be obtained when local atmospheric or hydrological mechanisms override the altitude effect (McGill et al., 2020).

3.4. Statistical analysis

Principal component analysis (PCA) and cluster analysis are valuable tools for investigating the spatial patterns of water geochemistry parameters in the analysis of surface water and groundwater (Yang et al., 2020). PCA integrates correlated variables to create new composite variables, enabling the reduction of numerous quantitative variables into a few variables. To identify the factors or sources responsible for variations in water quality among samples, PCA, using correlation coefficient matrices, was adapted to this study. Additionally, cluster analysis was employed to group water samples based on their water quality trends relative to each factor.

The normality of data was initially assessed using the Shapiro–Wilk test for each surface water sample collected during different sampling periods (Shapiro and Wilk, 1965). The MIW was collectively tested irrespective of the sampling period. The water quality data with non-normal distribution were logarithmically transformed. Subsequently, PCA was conducted for surface water and MIW to extract loading factors. Grouping based on the extracted factors was performed using cluster analysis. Hierarchical cluster analysis utilizing Ward's method with Euclidean distance was also applied in this study. MIW samples underwent PCA and cluster analysis

Table 1
δ^{18} O, δ^2 H, d-excess values, the physical and hydrochemical parameters of the surface water (W1–W29) and MIW (M1–M9) samples.

Sample Name		Elevation (m)	Calculated Recharge Elevation (m)	T (°C)	pH	EC (μS/cm)	Eh (mV)	$\delta^{18}O$ (‰)	δ^2H (‰)	d-excess (‰)
W1–W26	Min	70	153	2	5.0	26	270	−7.8	−51	11
(*n* = 51)	Max	205	273	22	8.1	158	566	−7.3	−45	14
	Mean	142	208	14	7.0	63	397	−7.5	−48	12
W27–W29	Min	22	-	7	7.3	146	288	−8.3	−55	5
(*n* = 6)	Max	31	-	15	9.1	158	549	−6.7	−49	13
	Mean	26	-	11	8.0	152	374	−8.0	−53	11
M1	Min			13	3.9	344	449	−7.9	−50	13
(*n* = 12)	Max			14	4.2	463	542	−7.8	−48	15
	Mean			14	4.1	408	517	−7.8	−49	14
M2	Min			13	3.5	491	500	−8.0	−51	13
(*n* = 4)	Max			15	3.7	611	598	−7.8	−49	14
	Mean			14	3.6	548	564	−7.9	−50	13
M3	Min			-	4.4	137	-	−7.7	−48	13
(*n* = 2)	Max			-	4.4	137	-	−7.6	−48	13
	Mean			-	4.4	137	-	−7.6	−48	13
M4	Min			14	3.3	528	-	−7.9	−49	13
(*n* = 2)	Max			14	3.3	528	-	−7.8	−49	14
	Mean			14	3.3	528	711	−7.8	−49	13
M5				14	3.6	422	688	−7.9	−50	13
M6	Min			14	3.8	215	-	−8.0	−50	14
(*n* = 2)	Max			14	3.8	215	-	−8.0	−50	14
	Mean			14	3.8	215	628	−8.0	−50	14
M7				-	-	-	-	−7.9	−49	14
M8	Min			14	5.8	348	273	−7.9	−49	13
(*n* = 4)	Max			15	6.1	482	313	−7.8	−49	14
	Mean			14	5.9	416	297	−7.8	−49	14
M9				-	-	-	-	−8.2	−51	15

The Eh values of MIW are exclusively listed for the samples in which Eh was measured on-site. For samples with only one measurement available, Eh was provided in the column of the mean value, excluding the maximum and minimum values.
Abbreviations: W, surface water; M, mine water; T, temperature; EC, electrical conductivity; $\delta^{18}O$, oxygen isotope; δ^2H, hydrogen isotope; d-excess, deuterium excess; Min, minimum; Max, maximum.

irrespective of the sampling period. M9 samples with no pH, EC, and Eh data were excluded from PCA and cluster analyses. These multivariate analyses were executed using the R package statistics (R. Core Team, 2021).

3.5. Mine-related information

The flow rate (m^3/min) of MIW for M1 and M2, and water temperature (℃) for the mixture of M1 and M2 water were recorded by the installed instrument at the treatment plant of MIW. The accumulated data of flow rate and water temperature from January 2019 to June 2021 were provided as mine-related data from the mine. Furthermore, 11 samples of M1 collected in July 2019 and monthly from February to November 2020 were subjected to water isotope analysis. These were compared with the precipitation data recorded at point A, approximately 12 km north of the mine area, to assess the effects of seasonal variation on the MIW. The distribution map of mine voids and geological data were integrated with geochemical and isotopic data of the MIW and surface water to elucidate the origin of MIW and its flow pathways.

3.6. Approach limitation

Based on the quality of both MIW and surrounding surface water, we segregated the components of MIW. Notably, the MIW from this mine exhibited elevated concentrations of F^- derived from CaF_2 and SO_4^{2-} attributing to the dissolution of sulfide minerals, surpassing those of the surrounding surface water. Thus, we aimed to achieve component separation by focusing on the F^- and SO_4^{2-} concentrations of MIW. While component separation and origin estimation of mine effluents based on regional water quality characteristics have been reported (Papp et al., 2017; Li et al., 2018; Huang et al., 2020; Chudy et al., 2021), our results and approach, focusing on the distinctive fluoride-rich nature of this mine, could be universally applicable to other mine sites with similar geological conditions. Moreover, variations in factors such as the spatial distribution of mine voids and the geological context can influence the patterns of water inflows into mine voids and groundwater characteristics (e.g., water quality, situation of stratification, residence time of groundwater). Consequently, such factors should also be considered when applying our approach to other mines.

4. Results and discussion

Tables 1 and 2 list the statistical summaries of 7 hydrochemical variables from the 57 surface water samples and 11 variables from the 29 MIW samples.

The flow rates from MIW for M1 and M2, along with the changing trend in water temperature of the combined MIW from M1 and M2, and in rainfall are illustrated in Fig. 3. Considering the convergence of MIW into M1 and M2 within this mine, M1 accounted for

Table 2
Concentration of major ions (mg/L) of the surface water (W1–W29) and MIW (M1–M9) samples.

Sample Name		pH	EC (μS/cm)	Na^+ (mg/L)	K^+ (mg/L)	Ca^{2+} (mg/L)	Mg^{2+} (mg/L)	Cl^- (mg/L)	HCO_3^- (mg/L)	SO_4^{2-} (mg/L)	NO_3^- (mg/L)	F^- (mg/L)	Total Fe (μg/L)
W1–W26	Min	5.0	26	2.0	0.1	1	1	3.0	0.5	2	0.3	0.0	0
(n = 51)	Max	8.1	158	8.9	9.6	29	5	11.3	49.5	61	25.2	3.0	209
	Mean	7.0	63	3.9	0.8	6	2	3.8	14.1	10	2.3	0.5	15
W27–W29	Min	7.3	146	10.4	1.5	14	4	9.6	39.7	18	4.6	0.1	0
(n = 6)	Max	9.1	158	11.4	1.8	16	4	11.3	46.7	20	7.1	0.1	12
	Mean	8.0	152	10.7	1.7	15	4	10.7	42.9	19	5.9	0.1	3
M1	Min	3.9	344	5.6	1.8	34	7	3.7	0.0	174	0.0	23.7	148
(n = 12)	Max	4.2	463	6.7	3.9	46	10	5.3	0.0	196	0.4	26.1	5384
	Mean	4.1	408	6.0	2.1	40	9	4.1	0.0	184	0.2	24.6	1933
M2	Min	3.5	491	5.7	2.4	37	10	3.8	0.0	226	0.0	36.6	249
(n = 4)	Max	3.7	611	5.9	2.6	45	14	4.0	0.0	273	0.1	38.8	18059
	Mean	3.6	548	5.7	2.5	41	12	3.9	0.0	254	0.1	37.7	8292
M3	Min	4.4	137	3.3	1.4	7	4	2.9	0.0	45	0.0	3.1	271
(n = 2)	Max	4.4	137	4.0	1.6	10	8	3.1	0.0	73	0.0	3.4	271
	Mean	4.4	137	3.6	1.5	8	6	3.0	0.0	59	0.0	3.3	271
M4	Min	3.3	528	8.3	2.9	37	11	4.7	0.0	229	0.1	23.3	4001
(n = 2)	Max	3.3	528	9.0	3.2	41	13	4.8	0.0	235	0.2	24.3	5459
	Mean	3.3	528	8.6	3.1	39	12	4.8	0.0	232	0.2	23.8	4730
M5		3.6	422	5.6	2.0	34	8	3.6	0.0	195	0.3	33.9	1878
M6	Min	3.8	215	4.2	2.3	10	5	3.9	0.0	79	0.1	8.5	259
(n = 2)	Max	3.8	215	4.3	2.3	11	5	4.0	0.0	79	0.1	8.8	622
	Mean	3.8	215	4.3	2.3	10	5	4.0	0.0	79	0.1	8.6	441
M7		-	-	6.0	1.9	45	9	3.6	0.0	196	0.0	24.6	290
M8	Min	5.8	348	5.6	1.8	37	7	3.6	0.9	175	0.0	23.1	217
(n = 4)	Max	6.1	482	6.5	2.1	44	9	3.6	0.9	191	0.2	25.2	12649
	Mean	5.9	416	6.1	2.0	42	8	3.6	0.9	186	0.1	24.4	5010
M9		-	-	9.6	4.2	84	24	3.7	0.0	429	0.2	52.0	290

For samples with only one measurement available, only the mean value was provided, excluding the maximum and minimum values.
Abbreviations: W, surface water; M, mine water; T, temperature; EC, electrical conductivity; Min, minimum; Max, maximum.

most of the MIW. Both M1 and M2 exhibited an increasing trend in flow rates following rainfall events, lasting from several weeks to months. This suggests the existence of a pathway for the infiltration of rainwater into the mine voids, subsequently discharged through the mine adits of M1 and M2. The flow rate of M1 showed a temporary increase following rain events, with a recorded minimum flow rate ranging from 0.37 to 0.50 m^3/min, gradually tending to approach the minimum flow rate. Such observations imply that the minimum value of MIW could stem from the continuous discharge of groundwater, and the flow rate of MIW can fluctuate due to the mixture of temporal rainwater. The temperature of M1 and M2 aggregated water decreased to approximately 11 °C in December and increased to 14 °C in August. Since the mean annual temperature of the study area is 13 °C, the water temperature of MIW might have experienced seasonal variations around 13 °C. Surface water temperatures ranged from 2 °C in February to 22 °C in August (Table 1). Assuming that surface water infiltrates into the mine voids during rainfall events, the influx of surface water into the mine voids is not substantial enough to increase the water temperature of MIW with that of surface water. Alternatively, the influx of groundwater, which maintains a stable temperature throughout the year, into the mine voids increased during rainfall events.

4.1. Hydrochemical and isotopic data for the surface water and the mining-influenced water samples

The surface water samples collected from W1 to W26 showed a pH range of 5.0–8.1 with an average value of 7.0 and EC ranging from 26 to 158 μS/cm with an average value of 63 μS/cm (Table 1). The EC measured at W27–W29 ranged from 146 to 158 μS/cm with an average value of 152 μS/cm. These EC values surpassed those recorded at W1–W26, attributable to the fact that the origin of W27–W29 was located beyond the study area. The mean concentrations of SO_4^{2-} and F^- ions in W1–W26 were 10 and 0.5 mg/L, respectively. The concentration of SO_4^{2-} above 10 mg/L and F^- concentration above 1.0 mg/L with a pH below 6.0 were recorded at W1–W3. Moreover, surface water samples from W15 and W21 showed F^- concentrations above 1.0 mg/L. Consequently, the influence of fluorite containing F^- within the ore deposit was inferred in the surface water observed at W1–W3, W15, and W21, as reported by Ikeda et al. (1983). The higher NO_3^- ion concentrations ranging from 11.4 to 25.2 mg/L at W17 than the average value of 2.3 mg/L for W1–W26 attributed to agricultural activities in the upstream area. The average temperatures recorded at point A during the 30 days preceding the sampling period were as follows: 3.5 °C in February 2020, 11.3 °C in November 2020, 25.8 °C in August 2021, and 19.9 °C in October 2021 (Japan Meteorological Agency). The average temperatures of the surface water samples collected from W1 to W26 were 6.1 °C in February 2020, 11.3°C in November 2020, 20.3°C in August 2021, and 16.4°C in October 2021. These values exhibited a similar trend with the average atmospheric temperatures during the corresponding periods, implying the mixture of precipitation into the surface water at W1–W26 during each sampling period.

The mean EC values were higher at M2 (548 μS/cm) than M1 (408 μS/cm) (Table 1). Moreover, the pH recorded at M2 ranging from 3.5 to 3.7 were notably lower than those observed at M1 ranging from 3.9 to 4.2. Higher concentrations of F^-, Mg^{2+}, and SO_4^{2-} were, additionally, detected at M2, indicating differences in water quality between M1 and M2. Conversely, the EC and concentrations of F^-, Mg^{2+}, and SO_4^{2-} at M3 and M6 were lower than those of other MIW samples. Although MIW at M8 and M9 converge at M7, the water quality at M7 was similar to that at M8, suggesting that MIW at M7 primarily comprises water originating from M8. Furthermore, the concentration of each element was higher at M9. These data imply distinct origins and flow pathways for each MIW sample.

4.1.1. Hydrochemical types of the surface water and the mining-influenced water samples using the Durov diagram

The results of analytical hydrochemical parameters were plotted on a Durov diagram (Ben Brahim et al., 2013; Durov, 1948) For

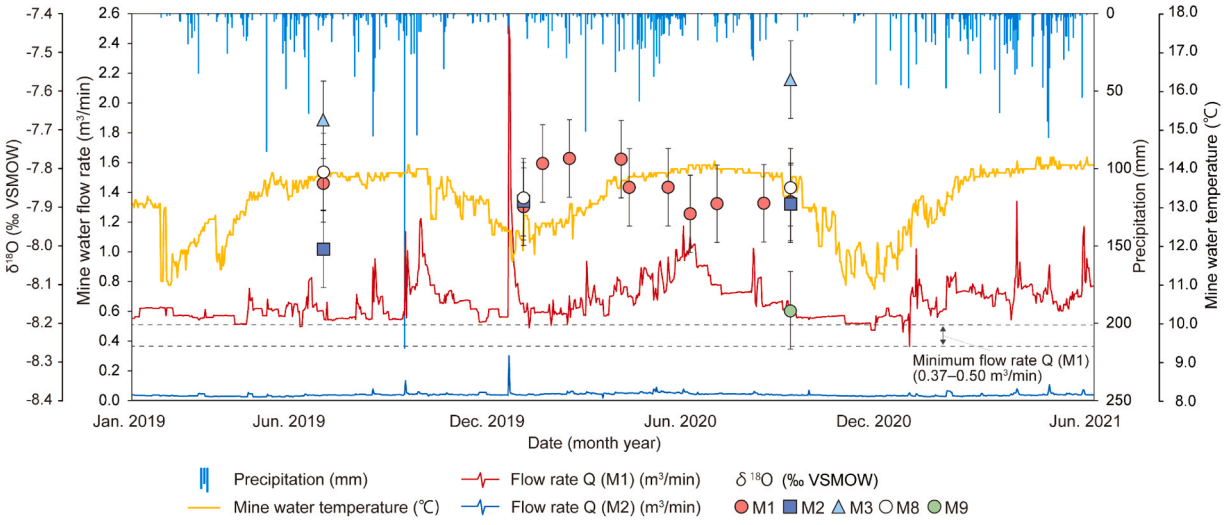

Fig. 3. Monitoring data with respect to the MIW flow rates Q (M1 and M2), precipitation, mine water temperature of the mixed MIW of M1 and M2, and change in $\delta^{18}O$ values at sites M1–M3, M8, and M9. The amount of precipitation was recorded at point A (Japan Meteorological Agency). Error bars in $\delta^{18}O$ indicate the analytical errors ±0.10 ‰.

cations, surface water samples were categorized into 1. sodium, 3. calcium, and 4. intermediate types along with the plots in 6. sulfate, 7. bicarbonate, and 8. intermediate types for anions (Fig. 4). In the central square, the majority of surface water samples were plotted in V. mixing reactions from various origins and VI. represent ion exchange waters. The sample at W14 was classified as type II, which is usually influenced by Ca^{2+} dissolution from the geological composition of the aquifer (primarily composed of calcite and gypsum), while W5–W8 were plotted near the boundary of V and IV, which is affected by mixing and reverse ion exchange reactions.

All MIW samples, excluding M3 and M6, were classified as type II. These findings indicate that the surface water and MIW in this area are primarily characterized by Ca^{2+}, HCO_3^-, and SO_4^{2-}, suggesting classification into the Ca-SO_4 and $CaHCO_3$ types, along with their intermediate types. The Ca-SO_4 type is a common water quality associated with mine areas rich in sulfide minerals, owing to acidification induced by FeS_2 in the ore deposits, and leaching of SO_4^{2-} (Chudy et al., 2021). The $CaHCO_3$ type is a characteristic often observed in the circulating groundwater of Japan. At W14, where the treated water from MIW merges, the water sample was distinguished by high concentrations of Ca^{2+} and SO_4^{2-}, exhibiting a similar trend in water quality with MIW. M3 and M6 were classified as the intermediate types and plotted near the surface water from W1 to W3.

MIW samples, excluding M8, were plotted at pH < 5.0, indicating the effects of acidification resulting from sulfide mineral dissolution. Moreover, surface water samples from W1 to W3 were plotted near M8, and exhibited a slightly different range with pH < 6 compared with other surface water samples, suggesting the influence of acidification from sulfide minerals contained in the ore deposits. Additionally, M8 was plotted near pH = 6, distinct from other MIW samples, which showed a differing pH value.

All MIW samples, except for M3 and M6 showed TDS exceeding 150 mg/L, while the others indicated TDS below 150 mg/L. The relatively low levels of dissolved substances in MIW from M3 and M6 suggested similarities to surface water from W1 to W3. Furthermore, M9 displayed the highest TDS concentration which was 600 mg/L.

4.1.2. Hydrochemical evolution of the surface water and the mining-influenced water samples in the study area

In the correlation between $Ca^{2+} + Mg^{2+}$ and $HCO_3^- + SO_4^{2-}$ (Fig. 5a), the dissolution of calcite ($CaCO_3$), dolomite ($MgCa(CO_3)_2$), and gypsum ($CaSO_4 \cdot 2\,H_2O$) was inferred for the water quality of surface water due to their plots along a 1:1 line, as indicated by their alignment along a 1:1 line (Rajmohan and Elango, 2004). The surplus of $HCO_3^- + SO_4^{2-}$ observed in MIW was attributed to the generation of SO_4^{2-} through the reaction of pyrite with water and oxygen. The molar ratio of Ca^{2+}/Mg^{2+} provides insights into the origins of Ca^{2+} and Mg^{2+} in groundwater from the points of the dissolution of calcite, dolomite, and silicate minerals (Fig. 5b) (Mayo and Loucks, 1995; Paul et al., 2019). The molar ratios of $Ca^{2+}/Mg^{2+} = 1$, $Ca^{2+}/Mg^{2+} > 1$, and $Ca^{2+}/Mg^{2+} > 2$ indicate the dissolution processes of dolomite, calcite, and silicates, respectively (Rajesh et al., 2012). The influence of calcite dissolution on the concentrations of Ca^{2+} and Mg^{2+} in the water was inferred for sites W5–W8, M3, and M6. W5–W8, which were located on the western slope of the mine, were plotted along the boundary of zones V and IV (Fig. 4), indicating a similar trend to the water quality of M3 and M6. These sites exhibited similar aqueous compositions. The remaining samples were influenced by silicate dissolution.

The SI for dolomite, calcite, and gypsum were computed using the GWB (Fig. 5e and f). Within the water samples of W1–W26, both dolomite and calcite exhibited undersaturation. Concurrently increasing with TDS, the SI values suggest the dissolution of dolomite and calcite contributing to the concentrations of Ca^{2+} and Mg^{2+}. Both surface water and MIW showed undersaturation (SI < 0) for gypsum, with SI values increasing along with the elevation of Ca^{2+} concentrations (Fig. 5f). This observation implies the contribution of gypsum dissolution to the supply of Ca^{2+}. Hence, the dissolution of calcite, dolomite, and gypsum is a significant factor influencing the aqueous geochemistry within the study area. Furthermore, the Ca^{2+}/Mg^{2+} ratios for M1 and M8 ranged from 4.2 to 5.3 (Fig. 5b). Considering that M1 represents a composite water sample comprising M3 to M9, M8 may constitute a significant component of M1. Although M2 is an outlet for MIW, excluding M1, the Ca^{2+}/Mg^{2+} ratios for M2 ranged from 3.2 to 3.7, diverging from those observed

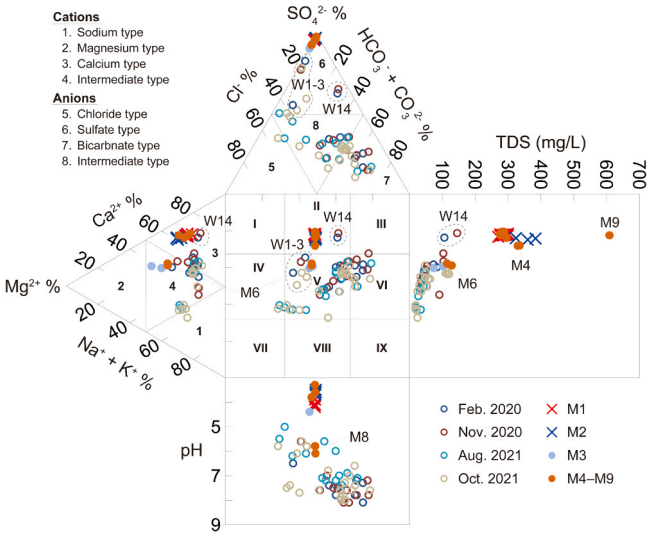

Fig. 4. Durov diagram with the hydrochemical types of the surface water and the mining-influenced water samples.

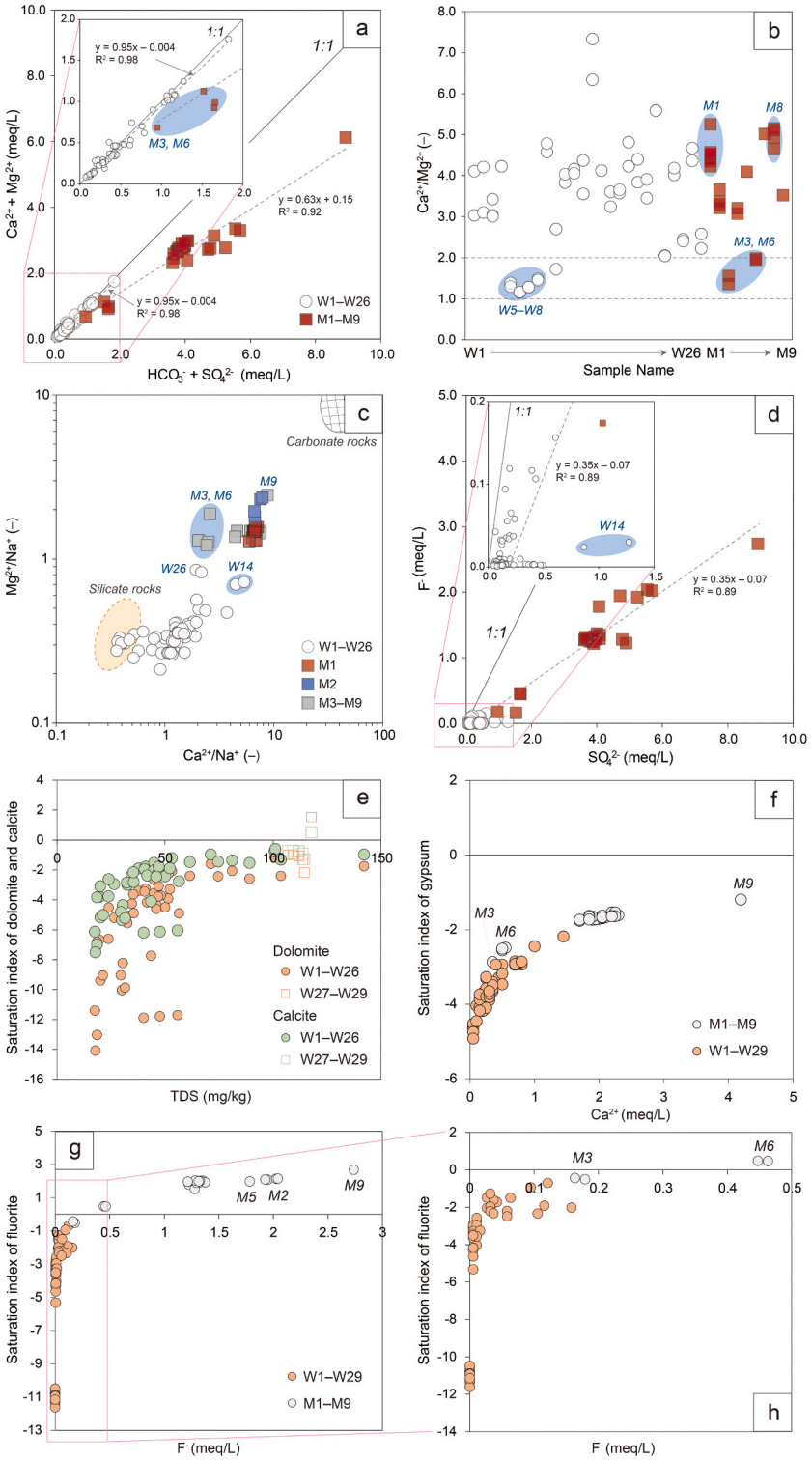

Fig. 5. Correlation between (a) $Ca^{2+} + Mg^{2+}$ vs. $HCO_3^- + SO_4^{2-}$, (b) variation in Ca^{2+}/Mg^{2+} ratios observed in surface water and MIW, (c) ratio of Mg^{2+}/Na^+ vs. Ca^{2+}/Na^+, (d) relationship between F^- and SO_4^{2-} concentrations, and saturation index (SI) of (e) dolomite ($MgCa(CO_3)_2$), calcite ($CaCO_3$), (f) gypsum ($CaSO_4 \cdot 2\,H_2O$), (g) fluorite (CaF_2), (h) the magnified view of (g).

for M1 and M8. This indicates that M2 comprises constituents distinct from those found in M8.

The plot of Mg^{2+}/Na^{+} vs. Ca^{2+}/Na^{+} shows rock-weathering sources for hydro-chemical characteristics of water with three end-members of carbonate, silicate, and evaporites (Fig. 5c) (Gaillardet et al., 1999). The area of evaporites is located outside the described range in the figure. Most surface water samples exhibited closer proximity to silicate rock compositions, suggesting that silicate weathering predominantly influences water quality. In contrast, MIW is situated between silicate and carbonate rock compositions. The plotting region corresponding to M3 and M6 differed from other MIW. This disparity arises due to the relatively reduced influence of Ca^{2+} originating from gypsum dissolution in M3 and M6. These samples potentially derive from precipitation through upper voids and thus experience lesser influence from mineral weathering.

The SI for gypsum in M3 and M6 is situated near surface water samples (Fig. 5f), further supporting the lesser impact of gypsum dissolution compared to other MIW.

The leaching of fluoride-bearing minerals within coal-bearing clastic rocks, attributed to mining activities, has been identified as a source of F^- contamination in water (Li et al., 2016). A noticeable correlation between F^- and SO_4^{2-} is evident, MIW plotting on the side of SO_4^{2-} excess relative to the 1:1 line (Fig. 5d). This is due to the co-occurrence of sulfides (such as FeS_2 and ZnS) and fluorite (CaF_2) within this ore deposit. The ore minerals in this mine include wolframite ((Fe, Mn) WO_4), chalcopyrite ($CuFeS_2$), pyrite (FeS_2), arsenopyrite (FeAsS), cassiterite (SnO_2), gangue consist of quart (SiO_2), lepidolite ($K_2(Li, Al)_5 \sim 6(Si, Al)_8O_{20}(OH, F)_4$), fluorite ($CaF_2$), Topaz ($Al_2SiO_4(F,OH)_2$), rhodochrosite ($MnCO_3$), as reported by Ikeda et al. in 1983. The ore deposit was identified within sandstone and shale formations sandwiched between two layers of chert. This ore deposit is exposed within the mine workings, suggesting the infiltration of seepage water into the workings through multiple fractures and fissures in the rock formations (Takase., 1958). As this seepage water flows through layers where pyrite and fluorite coexist, they contact with sulfide minerals such as FeS_2 and $CuFeS_2$, thereby generating SO_4^{2-}. Simultaneously, F^- leaches from fluorite and dissolves into the water, leading to a correlation between F^- and SO_4^{2-}, as reported in Takase., 1958; Li et al., 2016: during mine operation, similar concentrations were reported by seepage water exhibiting SO_4^{2-} and F^- concentrations which showed 0.36 and 0.13 meq/L, respectively (Takase, 1958).

At location W14, where treated MIW is mixed, it was plotted apart from the main cluster of MIW samples due to the removal of F^- resulting in lower concentrations, while SO_4^{2-} concentrations were slightly elevated compared with surface water (Fig. 5d).

The excess SO_4^{2-} for MIW samples was attributed to the continuous supply of SO_4^{2-} from the dissolution of gypsum, indicated by its undersaturation state (Fig. 5f), despite the absence of fluorite dissolution with the saturation conditions (Fig. 5g). Moreover, it is evident that as F^- concentrations increase, so does SI (Figs. 5g, h). All MIW samples, except for M3, exhibited $SI > 0$, indicating saturation, while both surface water and M3 showed undersaturation. Therefore, the dissolution of fluorite serves as the primary source of F^-. The dissolution of fluorite due to weathering and leaching of fluoride-bearing minerals and/or fluorite within the ore deposit has been reported elsewhere (Jha et al., 2013). MIW samples with $SI > 0$, excluding M3, likely experienced a greater influence from fluorite dissolution compared with surface water due to some degree of residence within the subsurface or the mine workings. On the other hand, M3 appeared to represent water with less influence from fluorite compared with other MIW samples, indicating a similar characteristic to surface water.

While iron is released into the water during the dissolution of pyrite, the form of iron in sampled water was examined. Surface water and MIW samples were plotted on the Eh-pH (Pourbaix) diagrams, which were constructed with the GWB12 (Fig. 6). Ferric hydroxide ($Fe(OH)_3$) was the dominant species in surface water. M8 was plotted within the region dominated by ferric hydroxide, while other MIW samples were situated within areas characterized by jarosite and, some were plotted in the area with ferrous ion. Surface water, influenced by the presence of carbonate and silicate minerals distributed within soil and rock formations during its surface flow, likely undergoes neutralization resulting in the precipitation of ferric hydroxide (Matthew et al., 2015). M8 is predominated by ferric hydroxide precipitation.

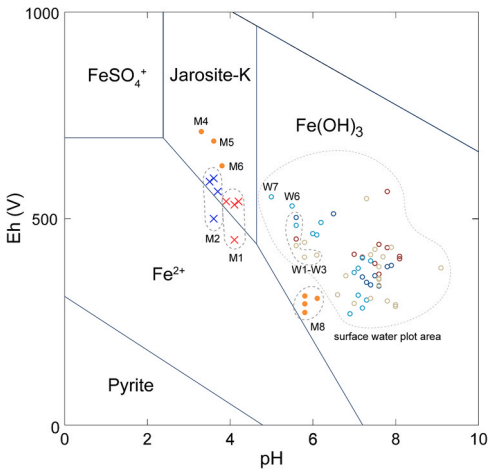

Fig. 6. Distribution of surface water and MIW samples on the Eh-pH (Pourbaix) diagram constructed with Geochemists Workbench at 14 °C (287.15 K) and 1.013 bars (101 kPa) pressure.

In contrast, aggregate waters from MIW such as M1 and M2 were controlled by jarosite-K. Considering the low dissolved oxygen (DO < 0.05 mg/L) observed in M8, the dissolution reactions of sulfide minerals mediated by dissolved oxygen are impeded, maintaining a pH near 6.0 and facilitating the presence of ferric hydroxide precipitation. Therefore, M8 likely represents groundwater with a certain degree of residence time, indicating a process wherein dissolved oxygen is gradually consumed during its flow.

4.1.3. Recharging area of the mining-influenced water

In the $\delta^{18}O$ vs. $\delta^{2}H$ diagram of the surface water and MIW (Fig. 7), plots originating outside the study area, specifically W27–W29, were excluded. The local meteoric water line (LMWL) of $\delta^{2}H = 8.02\delta^{18}O + 12.64$ in area A, approximately 34 km from the mine at a linear distance (Yabusaki et al., 2008), is represented by the local meteoric line with d = 11 and 15. Surface water samples from W1 to W26 were plotted along the LMWL with a slope of 4–6 (evaporation line), indicating their origin from rainwater and the influence of evaporation (Martinelli et al., 1996). Similarly, the plots of M1–M9 exhibited consistent trends along the linear regression line of $\delta^{2}H = 5.65\delta^{18}O - 4.90$ ($R^2 = 0.92$), possibly attributable to the evaporation effect during the process of precipitation infiltrating into the mine voids, flowing through the drainage within the voids, or both. The surface water samples from W1 to W26 showed varying plots based on the sampling periods, suggesting fluctuations attributable to seasonal variations in the isotopic composition of precipitation.

Conversely, the water isotopic values of M1 and M2 fell within the range of analytical errors, thereby precluding the observation of any obvious influence from seasonal variations.

The median $\delta^{18}O$ values of both MIW and surface water resided within distinct ranges falling below −7.8 ‰ and approximately above −7.6 ‰, respectively. This discrepancy, surpassing the analytical errors of ±0.1 ‰, may potentially be attributed to altitude effects (Clark and Fritz, 1997; Kong and Pang, 2016). Notably, the MIW exhibits isotopic signatures lighter than those of the surface water, suggesting a recharge source of MIW originating from precipitation at higher elevations compared with the surface water. MIW samples collected from M6 and M9 exhibited lighter values than the surface water, whereas those from M3 were plotted within an area near that of the surface water, with values exceeding −7.7 ‰. This suggests the presence of various mine drainage sources along with precipitation recharge across various elevation zones.

Due to the respective influences from ore deposits and anthropogenic sources, water samples W1–W3, W15, and W21, distinguished by elevated F^- concentrations, W14 as treated water, and W17, exhibiting high NO_3^- concentrations ranging from 11.4 to 25.2 mg/L, were omitted from altitude effect considerations. These distinct characteristics of the water samples were supported by the results of the PCA analysis in Section 4.2. The relationship between recharge elevation and water isotopes of the surface water is illustrated with isotopic values of the MIW (Fig. 8).

The results were plotted along the gradient of −0.3 (‰/per 100 m) for $\delta^{18}O$ values (Fig. 8a) and −2.0 (‰/per 100 m) for $\delta^{2}H$ values (Fig. 8b). These gradients reflect reasonable values being within the reported range for altitude effects in prior studies, ranging from −0.15 to −0.5 ‰ (‰/per 100 m) for $\delta^{18}O$ values (Clark and Fritz, 1997), and −0.1 to −0.5 ‰ (‰/per 100 m) for $\delta^{18}O$ values, along with −0.5 to −4.0 ‰ (‰/per 100 m) for $\delta^{2}H$ values (Jasechko, 2019). In terms of $\delta^{2}H$, certain water samples from W5 to W8 deviated from the shaded area. W5−W8, which were located on the western slope of the mine, exhibited distinct water quality compared to other surface water samples (Figs. 4 and 5b), suggesting potential influences on water isotopes, although details remain lacking. Estimation of the recharge elevation was calculated using the lower approximation line (y = −330x −2360) of the shaded area in $\delta^{18}O$;

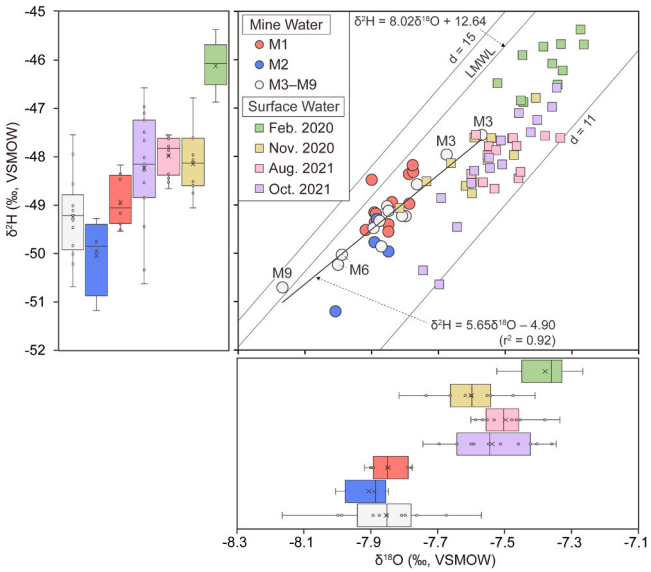

Fig. 7. The central figure describes $\delta^{18}O$ vs. $\delta^{2}H$ diagram of the surface water and MIW. The plots include the local meteoric water line (LMWL: $\delta^{2}H = 8.02\delta^{18}O + 12.64$ in area A as indicated by Yabusaki et al., 2008) and the linear regression line of MIW ($\delta^{2}H = 5.65\delta^{18}O - 4.90$, $R^2 = 0.92$) for reference. The plots on the left and bottom show box plots for various types of surface water and MIW, with the left plot representing $\delta^{2}H$ and the bottom plot representing $\delta^{18}O$. Different colors of box plot symbols indicate differences in types of surface water and MIW.

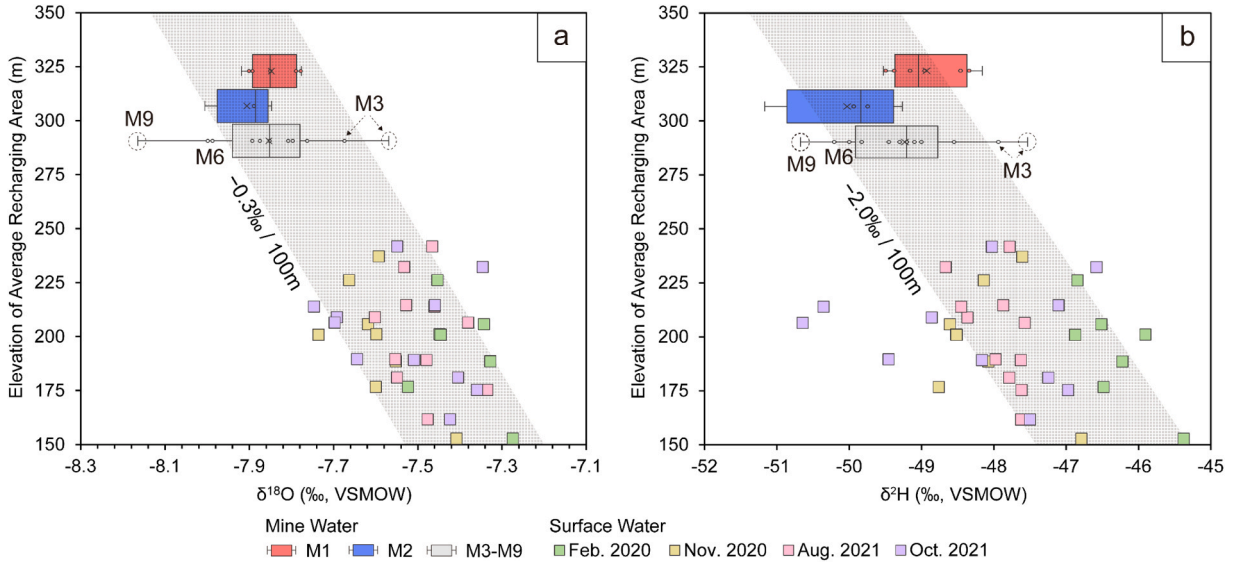

Fig. 8. Relationship between the average recharge elevation and (a) $\delta^{18}O$, and (b) $\delta^{2}H$. Different colors of box plot symbols indicate differences in types of MIW.

they indicated a minimum estimated recharging elevation of 160 m or higher for M3, 280 m for M6, and 340 m for M9. The average $\delta^{18}O$ value of M8 suggested an estimated recharge elevation of $\geq$ 220 m.

M3 was at the geological boundary between the sandstone and shale layers (Fig. 2), with the ground surface directly above at an elevation of 240 m, closest to the horizontal mine void at 170 m. Numerous large fractures, exceeding several meters in width, were observed within the alternating layers of sandstone and shale, sandwiched between two sheets of chert (Ikeda et al., 1983). It was inferred that water could readily pass through these fractures. Hence, rainfall recharging at an approximate altitude of 240 m above point M3 infiltrated into the mine voids, exhibiting a brief residence time before emerging from the ceiling at M3 as seepage water. This was supported by the estimated recharging elevation of M3, exceeding 160 m. Both M6 and M9 are expected to be linked to the upper voids U1–U3 (Fig. 1d), with the surface elevation of the distribution area of the mine horizontal voids U1–U3 standing at approximately 300 m. Given this context, it is plausible that precipitation recharge at the surface ground may percolate into M6 and M9 through these upper voids. This hypothesis was further supported by the estimated elevations of M6 and M9, which exceeded approximately 280 m. The upper tunnels U1–U3, to which M9 is likely connected, extended over a considerably broader area compared with the western upper tunnels linked to M6. Consequently, on the pathway flowing through these extensive upper tunnels, significant leaching may occur from the tunnel walls and rocks, potentially elevating TDS levels in M9. However, such speculation cannot be asserted based solely on the data collected in this study.

The correlation between the median of M1 and the altitude effect implies their origin from an elevation zone at least 230 m higher. As M8 was suggested to be dominant for M1 (Figs. 3 and 5b), the recharge elevation of M8 would similarly be at least 230 m higher, consistent with the estimated recharge elevation of 220 m for M8. Considering the hydrological pathway of M8, precipitation infiltrating through the sandstone and shale layers, characterized by faults and fractured zones, likely flows into the mine voids and flows out from shaft I at M8. In this scenario, infiltrating water within the mine voids undergoes some residence time, transitioning into groundwater, and subsequently flowing into the ground level mine voids from M8. This can be corroborated by the pH of approximately 6.0 observed at M8, alongside the presence of ferric hydroxide precipitate (Fig. 6).

4.1.4. Seasonal variations in surface water and the mining-influenced water

While seasonal variations in $\delta^{18}O$ are expected to appear in M1 when rainwater intermixes with MIW (Gat, 1996), the range of isotopic values was within the range of analytical errors. Yabusaki et al. (2008) reported a $\delta^{18}O$ value of 4.5 ‰ in area A (approximately 34 km from the mine, linearly) between February and October at an elevation of 275 m. The annual fluctuations in $\delta^{18}O$ and d-excess values were 6.8 ‰ and 12.8, respectively. The $\delta^{18}O$ and d-excess values of M1 exhibited a change of 0.1 ‰ and 1.5, respectively, during the corresponding period in 2020, a slight change compared with that reported by Yabusaki et al. (2008). Similar patterns were found in the $\delta^{2}H$ results. Despite the sampling of surface water at different times, the d-excess fluctuated within the range of d = 11–15 (Fig. 7). This indicates minimal seasonal variability, around 4, in the d-excess of surface water originating from precipitation in this region, suggesting an absence of isotopic seasonal variations in M1. Therefore, the disparity in isotopic compositions among surface water (Fig. 7 and Fig. 8), and MIW in M1–M9, can be attributed to differences in recharge elevations.

4.2. Component separation of MIW in this mine using PCA and cluster analysis

The PCA results showing 14 geochemical parameters derived from 57 surface water samples are summarized for each sampling

period in Table 3 and depicted in Fig. 9a, b, c, d, e, f, g, and h. The cluster analysis results involving 3 and 7 geochemical parameters from the same 57 surface water samples are illustrated in Fig. 9a', b', c', d', e', f', g', and h'. Fig. 9a', c', e', and g' present clusters categorized based on major dissolved constituents such as EC, Na^+, K^+, Ca^{2+}, Mg^{2+}, Cl^-, and HCO_3^- which were the predominant parameters extracted in PC1 of the PCA results. Meanwhile, Fig. 9b', d', f', and h' display clusters primarily influenced by parameters like SO_4^{2-}, NO_3^-, and F^-, which were the primary factors in PC3 and PC4 of the PCA results. Furthermore, the PCA and cluster analysis findings concerning 13 geochemical parameters derived from 16 MIW samples are provided (Table 4 and Fig. 10a and b). The cluster analysis results of 4 and 7 geochemical parameters from 16 MIW samples are also illustrated in Fig. 10a' and b', the left side of which shows clusters based on the major dissolved components EC, Na^+, K^+, Ca^{2+}, Mg^{2+}, Cl^-, and HCO_3^-, while the right side shows clusters based on pH, SO_4^{2-}, NO_3^-, and F^-.

Principal components (PC1–PC4) influencing the water quality of both surface water and MIW have been identified, accounting for 90.4 % of the variance in the original data in February 2020, 91.2 % in November 2020, 86.1 % in August 2021, and 90.2 % in October 2021. PC1 exhibited high loadings on EC, Na^+, K^+, Ca^{2+}, Mg^{2+}, Cl^-, and HCO_3^-. These major ions are associated with hydrochemical variables resulting from mineral weathering and water–rock interactions. During each sampling period, SO_4^{2-} and F^- were consistently extracted as principal components in PC2–PC4.

This phenomenon arises from the acidification reaction of water due to contact with sulfide minerals and the concurrent dissolution of CaF_2, leading to the simultaneous leaching of SO_4^{2-} and F^- (Fig. 5d and g, h).

Furthermore, during the sampling periods in November 2020 and October 2021, nitrate and potassium were extracted as principal components, indicating their close association with anthropogenic contamination sources such as farms and wastewater. The results from the sampling points of W27–W29, as depicted in Fig. 9a, c, a', and c', illustrated a distinct clustering of these samples from other surface water samples based on the trend of major dissolved components represented by PC1. This discrepancy is attributed to the origin of W27–W29 from outside the study area, which was consistent with their higher EC compared with other surface water samples. Treated water at W14 also exhibited distinctive characteristics in terms of SO_4^{2-} content, as indicated by PC2 (Fig. 9a) and PC4 (Fig. 9d), where it is plotted outside the range of other surface water samples. Surface water samples W17 and W26 were also plotted outside the range of other samples in PC3 and PC4 (Figs. 9b and d). This was due to the additional influence of nitrate from anthropogenic pollution and SO_4^{2-} from the mineral deposits. By focusing on the loadings of pH, SO_4^{2-}, and F^-, it is evident that surface water samples W1–3 and W15 were plotted in distinct ranges compared with other SW samples. W1–3 exhibited a different area of plotting based on the F^- concentration loading in PC2 (Fig. 9a, e, and g), PC4 (Fig. 9d). Similarly, W15 and W21 were plotted in

Table 3
Results of the factor loadings for 57 surface water samples using Principle Component Analysis (PCA).

	Feb., 2020				Nov., 2020			
	PC1	PC2	PC3	PC4	PC1	PC2	PC3	PC4
pH	0.16	**0.48**	0.26	0.00	0.20	0.01	0.21	**0.54**
EC	**0.33**	-0.20	0.17	0.00	**0.35**	-0.01	0.11	-0.20
Eh	-0.18	**-0.30**	0.23	**0.42**	0.03	**-0.58**	0.06	-0.23
$\delta^{18}O$	0.16	0.05	**-0.52**	**0.55**	0.19	-0.29	**-0.55**	-0.02
$\delta^{2}H$	0.29	0.10	**-0.38**	0.29	0.25	-0.27	**-0.45**	0.04
Na^+	**0.34**	0.06	-0.01	0.04	**0.34**	-0.02	-0.17	0.12
K^+	0.27	-0.11	-0.08	**-0.39**	0.24	**0.50**	-0.07	-0.04
Ca^{2+}	**0.31**	-0.16	**0.33**	0.14	**0.31**	-0.03	**0.32**	-0.18
Mg^{2+}	**0.33**	-0.11	0.22	0.04	**0.32**	-0.05	0.24	-0.11
Cl^-	**0.34**	-0.01	-0.19	-0.06	**0.33**	0.11	-0.24	0.01
HCO_3^-	**0.30**	0.25	0.19	0.18	**0.31**	-0.24	0.26	0.09
SO_4^{2-}	0.23	**-0.42**	0.24	0.11	0.25	0.04	0.21	**-0.48**
NO_3^-	0.22	-0.26	**-0.35**	**-0.45**	0.26	**0.40**	-0.23	-0.01
F^-	-0.14	**-0.52**	-0.13	0.13	-0.20	0.14	-0.18	**-0.56**
Eigenvalue	2.77	1.63	1.10	1.07	2.75	1.37	1.33	1.24
Cumulative % of variance	54.68	73.58	82.27	90.39	54.12	67.59	80.23	91.23
	Aug., 2021				Oct., 2021			
	PC1	PC2	PC3	PC4	PC1	PC2	PC3	PC4
pH	0.28	0.17	0.18	**0.35**	0.06	**0.47**	0.19	**0.44**
EC	**0.36**	-0.08	0.01	-0.11	**0.31**	-0.16	0.15	-0.01
Eh	**-0.32**	0.01	-0.23	-0.13	**-0.30**	-0.21	-0.22	0.14
$\delta^{18}O$	-0.13	-0.14	-0.24	**0.77**	**-0.34**	-0.09	-0.01	-0.05
$\delta^{2}H$	-0.12	-0.22	**0.38**	0.26	**-0.31**	-0.06	-0.13	-0.07
Na^+	**0.35**	0.12	0.05	0.06	**0.35**	-0.02	-0.04	0.14
K^+	**0.32**	-0.17	0.14	-0.10	**0.30**	-0.01	-0.17	**-0.57**
Ca^{2+}	**0.35**	-0.11	0.01	-0.13	**0.33**	-0.19	0.15	0.05
Mg^{2+}	**0.35**	0.08	0.01	-0.06	**0.32**	-0.10	-0.07	0.25
Cl^-	0.17	**0.37**	-0.27	**0.32**	0.25	-0.06	**-0.55**	-0.24
HCO_3^-	**0.34**	-0.01	-0.06	0.15	**0.32**	0.24	0.09	0.08
SO_4^{2-}	0.20	**-0.46**	**-0.36**	0.04	0.07	**-0.51**	0.27	0.18
NO_3^-	0.06	**0.33**	**-0.63**	-0.16	0.06	**-0.34**	**-0.52**	**0.50**
F^-	0.04	**-0.62**	-0.29	-0.03	-0.01	**-0.47**	**0.41**	-0.16
Eigenvalue	2.73	1.42	1.20	1.08	2.76	1.74	1.14	0.82
Cumulative % of variance	53.09	67.49	77.82	86.11	54.33	76.04	85.36	90.18

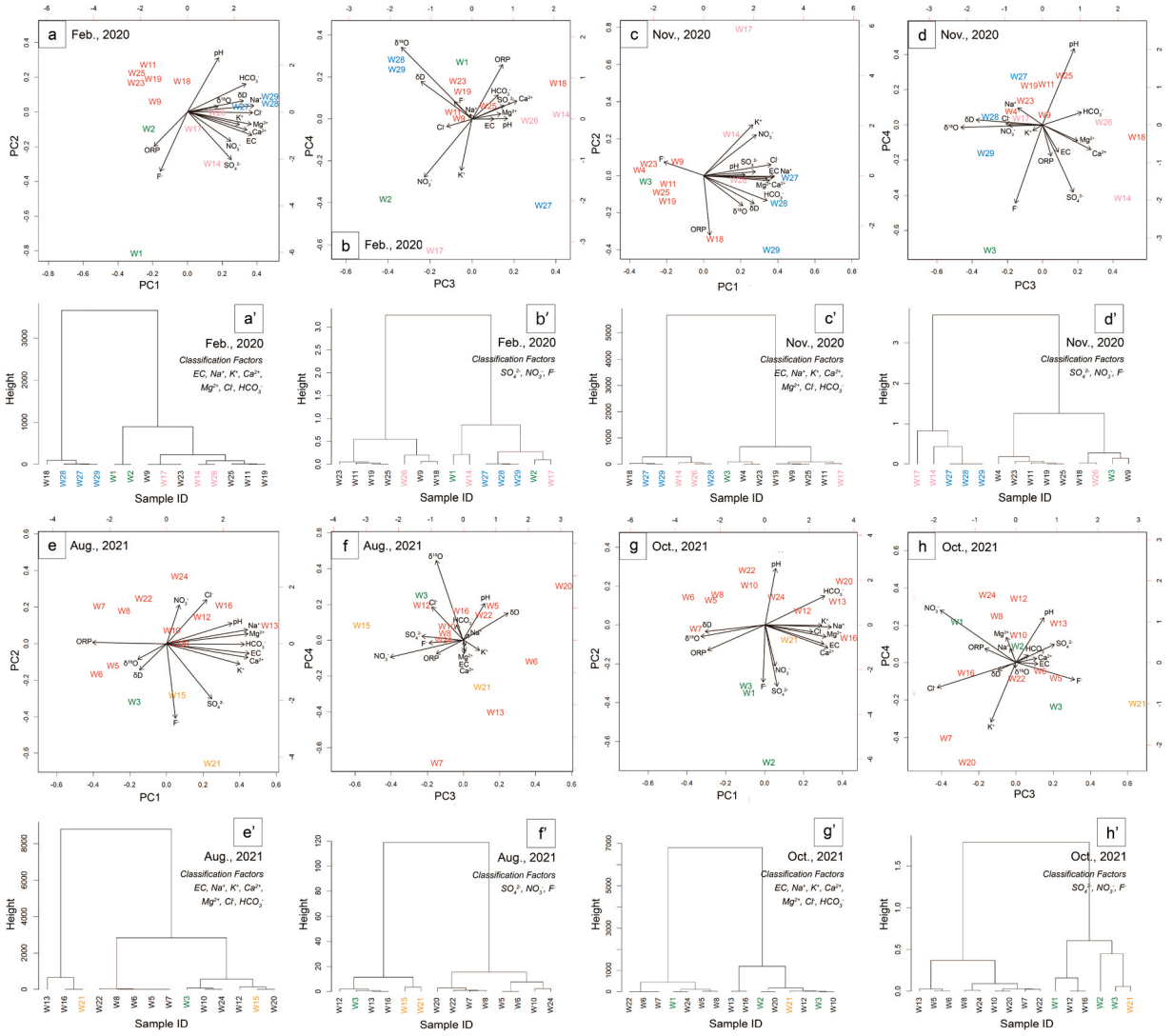

Fig. 9. Coordinates of principal component analysis and cluster analysis results based on water quality of 57 surface water samples.

different ranges in PC2 (Figs. 9e and g). These samples have all been influenced by either SO_4^{2-}, nitrate, or F^- and were classified into different clusters (Fig. 9b', d', f', h'). This was consistent with the distinct water quality characteristics exhibited by W1–W3 (Fig. 4). Additionally, during the estimation of recharge elevations (Fig. 8), the exclusion of W1–W3, W15, W17, and W21 due to the influence of mineral deposits or anthropogenic pollution is supported by the data.

PC1 accounted for 50.8 % of the variance, delineated by 13 chemical variables (Table 4). The water quality of MIW was primarily governed by Ca^{2+}, Mg^{2+}, SO_4^{2-}, and F^-, being supported by the findings in Fig. 5.

This entails the leaching of Ca^{2+} and Mg^{2+} from calcite and dolomite, the release of SO_4^{2-} from sulfide minerals, and the dissolution of F^- from fluorite. Within PC1, M3 and M6 were distinctly plotted in separate regions from other MIW samples (Fig. 10a), accompanied by a distinct clustering pattern (Fig. 10a'). This implies that based on water quality, M3 and M6 exhibited distinct characteristics compared with other MIW samples. PC2 signified an increase in pH and Ca^{2+} concentration alongside a decrease in Eh. Consequently, M8 was depicted in a distinct region from other MIW samples (Fig. 10a'). M8, characterized by DO levels below 0.05 mg/L, likely flows under reducing conditions with minimal dissolved oxygen presence, thereby inhibiting sulfide mineral oxidation and water acidification. As a result, M8 exhibited a higher pH compared with other MIW samples. Correspondingly, according to Fig. 5f, gypsum in M8 was under saturation, indicating longer groundwater residence times compared with other MIW samples. This increased Ca^{2+} concentrations based on gypsum dissolution in M8 samples.

In the classification focusing on pH, SO_4^{2-}, NO_3^-, and F^- which characterized the MIW of this mine, each MIW was categorized into distinct clusters (Fig. 10b'), which suggested diverse inflow pathways into the mine voids. PC3 and PC4 indicated the relationship between other dissolved components and water isotopes (Fig. 10b); however, further discussion on this is deemed unnecessary in this study since the discrepancy in isotopic values among MIWs, excluding M3, M6, and M9, is within the range of analytical errors.

Table 4
Results of the factor loadings for 16 mine-influenced water samples using PCA.

	MIW			
	PC1	PC2	PC3	PC4
pH	0.15	**0.54**	0.07	0.09
EC	**-0.37**	0.09	0.05	-0.07
Eh	-0.12	**-0.54**	-0.10	-0.26
$\delta^{18}O$	-0.19	-0.23	**0.51**	0.27
$\delta^{2}H$	-0.21	-0.24	0.54	0.18
Na^{+}	**-0.32**	0.20	-0.24	-0.09
K^{+}	-0.28	-0.17	**-0.33**	**0.43**
Ca^{2+}	**-0.33**	**0.32**	0.00	-0.07
Mg^{2+}	**-0.36**	0.09	0.04	-0.10
Cl^{-}	-0.24	-0.17	**-0.47**	**0.40**
SO_4^{2-}	**-0.37**	0.18	0.06	-0.08
NO_3^{-}	-0.13	-0.20	-0.11	**-0.67**
F^{-}	**-0.36**	0.15	0.16	-0.09
Eigenvalue	2.57	1.58	1.21	1.07
Cumulative % of variance	50.81	70.02	81.25	90.05

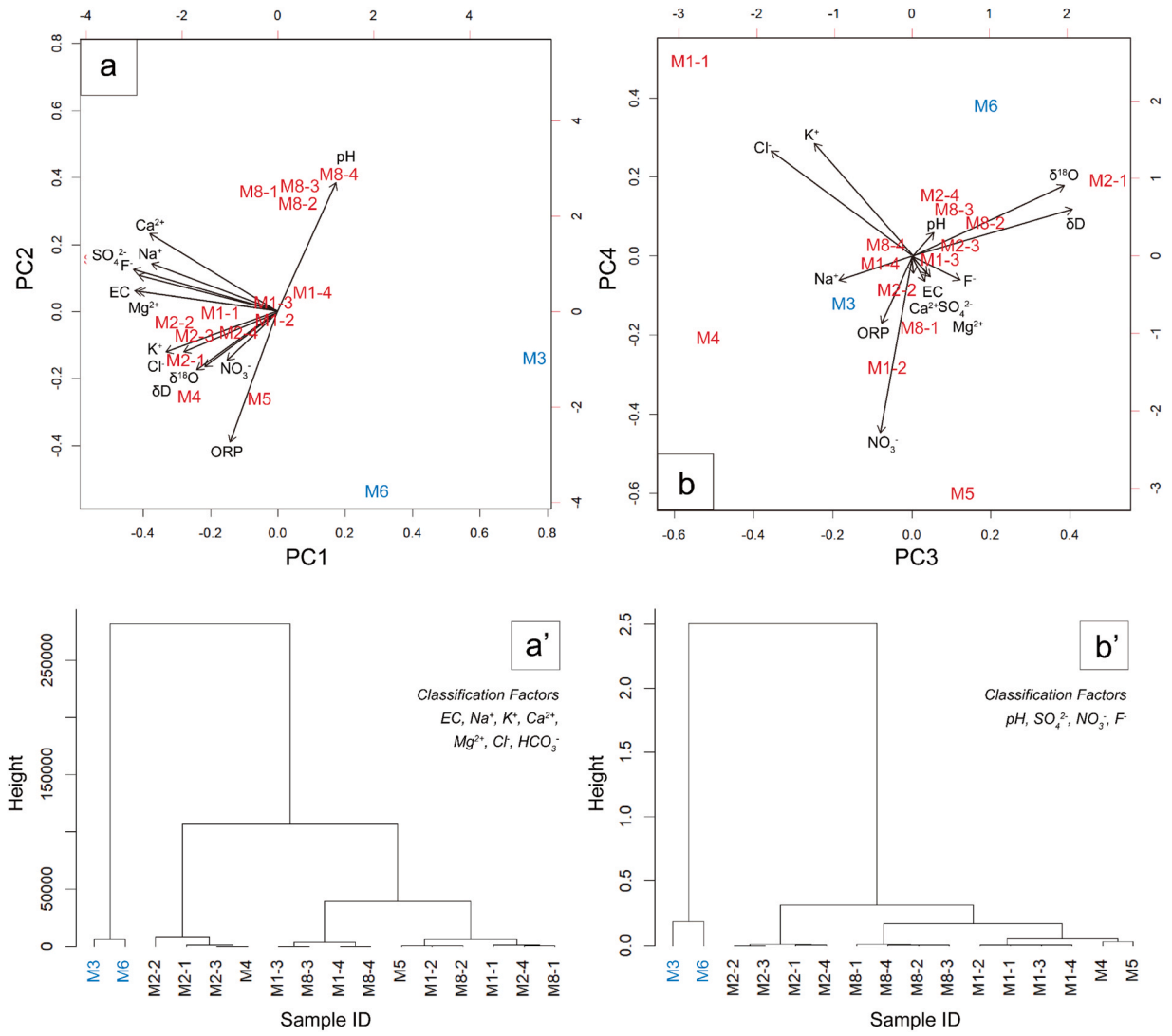

Fig. 10. Coordinates of principal component analysis and cluster analysis results based on water quality of 16 mine-influenced water samples.

4.3. Main constituents and flow pathways of MIW inflow

The water quality and isotopic analysis results showed that M3, M6, M8, and M9 exhibited distinct characteristics compared to the other MIW. The conceptual diagram of the inflow water for each MIW in this mine is illustrated in Fig. 11.

M3 represented seepage water from the ceiling, situated at the geological interface between the sandstone and shale layers. It is presumed to inflow through numerous large fractures within these layers, and faults, as indicated by the inflow water marked "C" in Fig. 11. The estimated recharging elevation for M3 was a minimum of $\geq$ 160 m, given the surface elevation directly above it is 240 m. This suggests that precipitation infiltrating the surface at this elevation promptly enters the mine voids. Similarly, M6 received water inflow via the upper voids U1–U3, as illustrated by inflow water labeled "B" in Fig. 11.

The estimated elevation for M6 exceeded 280 m, which was consistent with the topography where the northwestward U1–U3 mine voids, presumed pathways for inflowing water to M6, were situated at an altitude exceeding 300 m. Both M3 and M6 received infiltrated precipitation from the surface over short durations, being similar to the characteristics of surface water from W1 to W3, exhibiting low levels of dissolved substances. In particular, M3 displayed minimal influence from fluorite, suggesting water ingress through fractures over short periods. M8 is believed to be fed by subsurface mine water that has not been exposed to oxygen, unlike other MIW, flowing through shaft I to the ground level mine voids (inflow water D in Fig. 11). The estimated recharge elevation of M8 was $\geq$ 220 m. Given that the entire mountainous area where the mine voids are located matches this elevation range, it is plausible that precipitation infiltrating the entire mountain penetrates underground to become groundwater, flowing from M8 into the ground level voids. M9 exhibited the highest concentrations of F^- and TDS. Considering its connection to the northeast upper voids U1–U3, MIW from M9 may encounter sulfide minerals and fluorite-bearing minerals during the transit through the upper mine voids over a certain period, resulting in the leaching of SO_4^{2-} and F^- (inflow water B in Fig. 11). The estimated elevation of M9 exceeded 340 m. Additionally, M9 demonstrated the lightest water isotopic values among the MIW, and given that the northeastern upper voids are situated underground at an elevation of around 300 m, it is reasonable to infer that M9 originated from precipitation percolating at such relatively higher elevations and entering the mine voids.

The stratification phenomenon, characterized by the overlapping of water bodies with distinct physicochemical properties, was observed in submerged mines (Mugova and Wolkersdorfer, 2022; Nuttall and Younger, 2004). In such cases, a phenomenon known as the barrier effect has been reported, wherein underground MIW segregates into distinct water bodies: the upper regions of the workings, characterized by low mineralization (referred to as "cold fresh (CF)" water), and the lower portions, exhibiting higher mineralization (referred to as "warm mineralized (WM)" water). In this study, several remnants from past mining activities, including collapsed structures and machinery, were present around shaft I, making it challenging to safely conduct vertical depth-specific sampling and assessments, thus leaving the deeper stratification status unknown. On the other hand, we observed a consistent outflow, denoted as M8, originating from shaft I, with distinct characteristics compared with other MIW, with dissolved oxygen levels consistently below 0.05 mg/L. Given its meteoric water origin, it is presumed that precipitation infiltrates one of the stratified layers transforming into groundwater, subsequently flowing from M8 into the ground level mine voids. As the relatively stable water quality of the mine drainage is treated at this mine, it is inferred that M8, with consistent water quality, comprises most mine discharge. However, from the findings within this investigation, it remains unclear which flow—whether it be the infiltration from upper mine voids (M3, M6, M9) or the groundwater M8—responds to an increase in rainfall events. Clarifying the mechanisms underlying the increased flow of this MIW would provide valuable insights for mine effluent treatment.

The barrier effect of stratification, which separates groundwater discharged from flooded underground mine workings, reduces the volume of mineralized water from the mine and may consequently reduce the need for mine water treatment (Mugova and Wolkersdorfer, 2022; Wolkersdorfer et al., 2016).

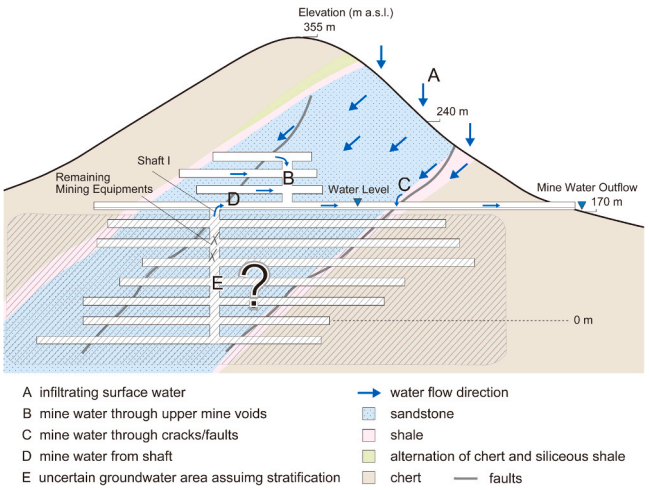

Fig. 11. Conceptual model of the main inflows into mine voids in this underground mine.

In cases where the volume of treated MIW increases with higher groundwater volume, which shows stable water quality, mitigation measures focused solely on the changing volume of MIW could be implemented. To achieve this goal, future investigations should include an examination of the flow model of groundwater M8, long-term monitoring of M8's flow rate and water quality, as well as depth-specific surveys into the underground from accessible sampling points and exploration of potential methodologies that can be implemented safely.

5. Conclusions

The study aimed to understand the composition of MIW in legacy mines in central Japan, crucial for treating mine wastewater and addressing sudden changes in water quality and MIW volume due to climate events.

We found MIW primarily consisted of two main components: infiltrating water rapidly passing through upper mine voids to reach the mine void at ground level, and groundwater that undergoes some degree of residence time before flowing into the ground level void from shaft I. Component separation relied on MIW characteristics, specifically F^- and SO_4^{2-} concentrations, supported by a water quality model using the GWB. Water isotope analysis revealed differences in elevation recharge areas of MIW, complementing the results of component separation. Stratification in flooded mines poses challenges, emphasizing the need for vertical surveys and innovative methods that can be safely implemented to comprehend deep underground conditions, essential for investigating groundwater flow pathways and long-term variations in MIW. These insights are essential for disaster response and wastewater management in the context of climate events.

CRediT authorship contribution statement

Shingo Tomiyama: Writing – review & editing, Validation, Investigation. **Saburou Yamagata:** Validation, Supervision, Resources. **Shinji Matsumoto:** Writing – review & editing, Writing – original draft, Validation, Methodology, Investigation, Funding acquisition, Formal analysis, Data curation, Conceptualization. **Taiki Katayama:** Writing – review & editing, Validation, Investigation. **Tetsuo Yasutaka:** Validation, Investigation, Funding acquisition.

Declaration of Competing Interest

The authors declare that they have no known competing financial interests or personal relationships that could have appeared to influence the work reported in this paper.

Data availability

Data will be made available on request.

Acknowledgments

We are very grateful to the staff of the Mitsubishi Materials Corporation and the Eco-Management Corporation for their help, advice, and cooperation with sampling during this study and providing the mine-related data. This research was financially supported by the Research Laboratory on Environmentally Conscious Developments and Technologies (E-code) at the National Institute of Advanced Industrial Science and Technology (AIST).

Appendix A. Supporting information

Supplementary data associated with this article can be found in the online version at doi:10.1016/j.ejrh.2024.101856.

References

Ben Brahim, F., Makni, J., Bouri, S., 2013. Properties of geothermal resources in Kebilli region, Southwestern Tunisia. Environ. Earth Sci. 69 (2013), 885–897. https://doi.org/10.1007/s12665-012-1974-7.

Bethke, C.M., Farrell, B., Yeakel. S., 2022. The Geochemist's Workbench Release 12: GWB Essentials Guide Technical Report. Date accessed: December 12th, 2023. https://www.gwb.com/pdf/GWB12/GWBessentials.pdf.

Blowes, D.W., Ptacek, C.J., Jambor, J.L., Weisener, C.G., 2003. 9.05 - The Geochemistry of Acid Mine Drainage, editor(s): Holland H.D., Turekian K.K (Pergamon). Treatise Geochem. 149–204. https://doi.org/10.1016/B0-08-043751-6/09137-4.

Chudy, K., Worsa-Kozak, M., Wójcik, A., Wolkersdorfer, C., Drzewicki, W., Konsencjusz, D., Szyszka, D., 2021. Chemical variations in mine water of abandoned pyrite mines exemplified by the Colorful Lakes in Wieściszowice, Sudetes Mountains, Poland. J. Hydrol. 38, 100974 https://doi.org/10.1016/j.ejrh.2021.100974.

Clark, I., Fritz, P., 1997. Environmental isotopes in hydrogeology. CRC Press, p. 328.

Dansgaard, W., 1964. Stable isotopes in precipitation. Tellus 16, 436–468. https://doi.org/10.1111/j.2153-3490.1964.tb00181.x.

Douglas, M., Clark, I.D., Raven, K., Bottomley, D., 2000. Groundwater mixing dynamics at a Canadian Shield mine. J. Hydrol. 235, 88–103. https://doi.org/10.1016/S0022-1694(00)00265-1.

Doveri, M., Natali, S., Franceschi, L., Menichini, M., Trifirò, S., Giannecchini, R., 2021. Carbonate aquifers threatened by legacy mining: Hydrodynamics, hydrochemistry, and water isotopes integrated approach for spring water management. J. Hydrol. 593, 125850 https://doi.org/10.1016/j.jhydrol.2020.125850.

Durov, S.A., 1948. Classification des eaux naturelles et la représentation graphique de leur composition. Dokl. Akad. Nauk. S. S. S. R. t. 59, 87–90.
El Fahem, M., Benzaouak, A., Zouiten, H., Serghini, A., Fekhaoui, M., 2021. Hydrogeochemical assessment of mine water discharges from mining activity. Case of the Haut Beht mine (central Morocco). AIMS Environ. Sci. 8, 60–85. https://doi.org/10.3934/environsci.2021005.
Gaillardet, J., Dupré, B., Louvat, P., Allègre, C.J., 1999. Global silicate weathering and CO2 consumption rates deduced from the chemistry of large rivers. Chem. Geol. 159, 3–30. https://doi.org/10.1016/S0009-2541(99)00031-5.
Gat, J.R., 1996. Oxygen and hydrogen isotopes in the hydrologic cycle. Annu. Rev. Earth Planet. Sci. 24, 225–262. https://doi.org/10.1146/annurev.earth.24.1.225.
Hamabe, S., Yano, T., 1976. Geological structure of the Kamaishi mining district, Iwate Prefecture. Jpn. J. Min. Geol. 26, 93–104 (in Japanese).
Hardy, S.D., Koontz, T.M., 2008. Reducing nonpoint source pollution through collaboration: policies and programs across the U.S. States. Environ. Manag. 41, 301–310. https://doi.org/10.1007/s00267-007-9038-6.
Huang, H., Chen, Z., Wang, T., Zhou, G., Martin, J.B., Zhang, L., Meng, X., 2020. Origins and mixing contributions of deep warm groundwater in a carbonate-hosted ore deposit, Sichuan-Yunnan-Guizhou Pb-Zn triangle, southwestern China. J. Hydrol. 590, 125400 https://doi.org/10.1016/j.jhydrol.2020.125400.
Ikeda, N., Hida, H., Noguchi, K., Fujiwara, M., 1983. Geology and ore deposits of the Takatori tungsten mine, Ibaraki Prefecture, Central Japan with special reference to the fracture system. Min. Geol. 33, 97–114 (in Japanese).
Iwasaki, Y., Fukaya, K., Fuchida, S., Matsumoto, S., Araoka, D., Tokoro, C., Yasutaka, T., 2021. Projecting future changes in element concentrations of approximately 100 untreated discharges from legacy mines in Japan by a hierarchical log-linear model. Sci. Total Environ. 786, 147500 https://doi.org/10.1016/j.scitotenv.2021.147500.
Japan Meteorological Agency. Past weather data. Date accessed: October 8th, 2022. https://www.data.jma.go.jp/gmd/risk/obsdl/. (in Japanese).
Jasechko, S., 2019. Global isotope hydrogeology–Review. Rev. Geophys. 57, 835–965. https://doi.org/10.1029/2018RG000627.
Jha, S.K., Singh, R.K., Damodaran, T., Mishra, V.K., Sharma, D.K., Rai, D., 2013. Fluoride in groundwater: toxicological exposure and remedies. J. Toxicol. Environ. Health, Part B. 16, 52–66. https://doi.org/10.1080/10937404.2013.769420.
Koide, R., Tokoro, C., Murakami, S., Adachi, T., Takahashi, A., 2012. A model for prediction of neutralizer usage and sludge generation in the treatment of acid mine drainage from abandoned mines: case studies in Japan. Mine Water Environ. 31, 287–296. https://doi.org/10.1007/s10230-012-0200-x.
Kong, Y.L., Pang, Z.H., 2016. A positive altitude gradient of isotopes in the precipitation over the Tianshan Mountains: effects of moisture recycling and sub-cloud evaporation. J. Hydrol. 542, 222–230. https://doi.org/10.1016/j.jhydrol.2016.09.007.
Levy, Z.F., Fram, M.S., Faulkner, K.E., Alpers, C.N., Soltero, E.M., Taylor, K.A., 2020. Effects of montane watershed development on vulnerability of domestic groundwater supply during drought. J. Hydrol. 583, 124567 https://doi.org/10.1016/j.jhydrol.2020.124567.
Li, X., Wu, P., Han, Z., 2016. Sources, distributions of fluoride in waters and its influencing factors from an endemic fluorosis region in central Guizhou, China. Environ. Earth Sci. 75, 981. https://doi.org/10.1007/s12665-016-5779-y.
Li, X., Wu, P., Han, Z., Zha, X., Ye, H., Qin, Y., 2018. Effects of mining activities on evolution of water quality of karst waters in Midwestern Guizhou, China: evidences from hydrochemistry and isotopic composition. Environ. Sci. Pollut. Res. 25, 1220–1230. https://doi.org/10.1007/s11356-017-0488-y.
Martinelli, L.A., Victoria, R.L., Sternberg, L.S., Ribeiro, A., Moreira, M.Z., 1996. Using stable isotopes to determine sources of evaporated water to the atmosphere in the Amazon Basin. J. Hydrol. 183, 191–204. https://doi.org/10.1016/0022-1694(95)02974-5.
Matthew, B.J.L., Michael, C.M., Jeffrey, G.B., John, L.J., Carol, J.P., David, W.B., 2015. Geochemical and mineralogical aspects of sulfide mine tailings. Appl. Geochem. 57, 157–177. https://doi.org/10.1016/j.apgeochem.2015.01.009.
Mayo, A.L., Loucks, M.D., 1995. Solute and isotopic geochemistry and ground water flow in the central Wasatch Range, Utah. J. Hydrol. 172, 31–59. https://doi.org/10.1016/0022-1694(95)02748-E.
McGill, L.M., Steel, E.A., Brooks, J.R., Edwards, R.T., Fullerton, A.H., 2020. Elevation and spatial structure explain most surface-water isotopic variation across five Pacific Coast basins. J. Hydrol. 583, 124610 https://doi.org/10.1016/j.jhydrol.2020.124610.
Mugova, E., Wolkersdorfer, C., 2022. Density stratification and double-diffusive convection in mine pools of flooded underground mines – A review. Water Res 214, 118033. https://doi.org/10.1016/j.watres.2021.118033.
Newman, C., Agioutantis, Z., Leon, G.B., 2017. Assessment of potential impacts to surface and subsurface water bodies due to longwall mining. Int. J. Min. Sci. Technol. 27, 57–64. https://doi.org/10.1016/j.ijmst.2016.11.016.
Nishimoto, N., Yamamoto, Y., Yamagata, S., Igarashi, T., Tomiyama, S., 2021. Acid mine drainage sources and impact on groundwater at the Osarizawa Mine, Japan. Minerals 11, 998. https://doi.org/10.3390/min11090998.
Nordstrom, D.K., Blowes, D.W., Ptacek, C.J., 2015. Hydrogeochemistry and microbiology of mine drainage: an update. Appl. Geochem. 57, 3–16. https://doi.org/10.1016/j.apgeochem.2015.02.008.
Northey, S.A., Mudd, G.M., Werner, T.T., Haque, N., Yellishetty, M., 2019. Sustainable water management and improved corporate reporting in mining. Water Resour. Ind. 21, 100104 https://doi.org/10.1016/j.wri.2018.100104.
Nuttall, C.A., Younger, P.L., 2004. Hydrochemical stratification in flooded underground mines: an overlooked pitfall. J. Contam. Hydrol. 69, 101–114. https://doi.org/10.1016/S0169-7722(03)00152-9.
Ogasawara, M., Seki, Y., Murao, S., Kodama, T., Tsukimura, K., Nakajima, T., 1993. Petrological and geochemical characteristics of aplite found near the Takatori tin-tungsten deposit in Japan and its relationship to mineralization. J. Mineral. Petrol. Econ. Geol. 88, 239–246. https://doi.org/10.2465/ganko.88.239.
Papp, D.C., Cociuba, I., Baciu, C., Cozma, A., 2017. Origin and geochemistry of mine water and its impact on the groundwater and surface running water in post-mining environments: Zlatna Gold Mining Area (Romania). Aquat. Geochem. 23, 247–270. https://doi.org/10.1007/s10498-017-9321-y.
Paul, R., Brindha, K., Gowrisankar, G., Tan, M.L., Singh, M.K., 2019. Identification of hydrogeochemical processes controlling groundwater quality in Tripura, Northeast India using evaluation indices, GIS, and multivariate statistical methods. Environ. Earth Sci. 78, 470. https://doi.org/10.1007/s12665-019-8479-6.
Peachey, E.J., 2004. The Aral Sea basin crisis and sustainable water resource management in Central Asia. J. Publ. ıC. Int. Aff. -Prince 15, 1–20.
Pourbaix, M., 1966. Atlas of electrochemical equilibria in aqueous solutions (English edition), Pergamon press, Oxford, 644p.
Qin, W., Han, D., Song, X., Liu, S., 2021. Environmental isotopes ($\delta^{18}O$, $\delta^{2}H$, and ^{222}Rn) and hydrochemical evidence for understanding rainfall-surface water-groundwater transformations in a polluted karst area. J. Hydrol, 592, 125748. https://doi.org/10.1016/j.jhydrol.2020.125748.
R. Core Team, 2021. R: A language and environment for statistical computing. R Foundation for Statistical Computing, Vienna. https://www.r-project.org.
Rajesh, R., Brindha, K., Murugan, R., Elango, L., 2012. Influence of hydrogeochemical processes on temporal changes in groundwater quality in a part of Nalgonda district, Andhra Pradesh, India. Environ. Earth Sci. 65, 1203–1213. https://doi.org/10.1007/s12665-011-1368-2.
Rajmohan, N., Elango, L., 2004. Identification and evolution of hydrogeochemical processes in the groundwater environment in an area of the Palar and Cheyyar River Basins. South. India Environ. Geol. 46, 47–61. https://doi.org/10.1007/s00254-004-1012-5.
Seki, Y., 1989. A hydrogeochemical exploration using fluoride in stream waters an example of the Takatori Sn-W deposit, Ibaraki Prefecture, Central Japan. J. Min. Geol. 39, 311–323 (in Japanese).
Shapiro, S.S., Wilk, M.B., 1965. An Analysis of Variance Test for Normality (Complete Samples). Biometrika 52, 591–611.
Skousen, J., Zipper, C.E., Rose, A., Ziemkiewicz, P.F., Nairn, R., McDonald, L.M., Kleinmann, R.L., 2017. Review of passive systems for acid mine drainage Treatment. Mine Water Environ. 36, 133–153. https://doi.org/10.1007/s10230-016-0417-1.
Sracek, O., Kříbek, B., Mihaljevič, M., Majer, V., Veselovský, F., Vencelides, Z., Nyambe, I., 2012. Mining-related contamination of surface water and sediments of the Kafue River drainage system in the Copperbelt district, Zambia: an example of a high neutralization capacity system. J. Geochem. Explor. 112, 174–188. https://doi.org/10.1016/j.gexplo.2011.08.007.
Takase, K., 1958. Geochemical prospecting in the Yamizo mountain range, Ibaraki prefecture (part II)–on the wolframite deposit of Takatori mine (No. I). Dep. Bull. Pap. 7, 139–148.
Taylor J.S., Pape S., Murphy N., 2005. A summary of passive and active treatment technologies for acid and metalliferous drainage (AMD), in: Proceedings of the 5th Australian Workshop on Acid Drainage, Fremantle, Western Australia, Aug 29–31, pp. 1–49.
Trumm, D., 2010. Selection of active and passive treatment systems for AMD—flow charts for New Zealand conditions. N. Z. J. Geol. Geophys. 53, 195–210. https://doi.org/10.1080/00288306.2010.500715.

Valkanas, M.M., Trun, N.J., 2018. A seasonal study of a passive abandoned coal mine drainage remediation system revealed three distinct zones of contaminant levels and microbial communities. MicrobiologyOpen 7, e00585. https://doi.org/10.1002/mbo3.585.

Wang, X., Gao, Y., Jiang, X., Zhang, Q., Liu, W., 2021. Analysis on the characteristics of water pollution caused by underground mining and research progress of treatment technology. Adv. Civ. Eng. 2021, 1–14. https://doi.org/10.1155/2021/9984147.

Wolkersdorfer, C., Shongwe, L., Schmidt, C., 2016. Can natural stratification prevent pollution by acid mine drainage? C. Drebenstedt, M. Paul (Eds.), IMWA 2016 – Mining Meets Water – Conflicts and Solutions TU Bergakademie Freiberg, Leipzig, German (2016), pp. 115-121.

Yabusaki, S., Tase, N., Tsujimura, M., Hayashi, Y., 2008. Characteristics of stable isotopes in precipitation at the south slope of Mt. Tsukuba. Bull. Terr. Environ. Res. Cent. Univ. Tsukuba 9, 15–23 (in Japanese).

Yang, J., Ye, M., Tang, Z., Jiao, T., Song, X., Pei, Y., Liu, H., 2020. Using cluster analysis for understanding spatial and temporal patterns and controlling factors of groundwater geochemistry in a regional aquifer. J. Hydrol. 583, 124594 https://doi.org/10.1016/j.jhydrol.2020.124594.

Yoon, T., Rhodes, C., Shah, F.A., 2015. Upstream water resource management to address downstream pollution concerns: a policy framework with application to the Nakdong River basin in South Korea. Water Resour. Res. 51, 787–805. https://doi.org/10.1002/2013WR014201.

Younger, P.L., 2001. Mine water pollution in Scotland: nature, extent and preventative strategies. Sci. Total Environ. 265, 309–326. https://doi.org/10.1016/S0048-9697(00)00673-2.

Zheng, L., Chen, X., Dong, X., Wei, X., Jiang, C., Tang, Q., 2019. Using $\delta^{34}S–SO_4$ and $\delta_{18}O–SO_4$ to trace the sources of sulfate in different types of surface water from the Linhuan coal-mining subsidence area of Huaibei, China. Ecotoxicol. Environ. Saf. 181, 231–240. https://doi.org/10.1016/j.ecoenv.2019.06.001.